NAR Genomics and Bioinformatics, 2025, **7**, lqaf071
https://doi.org/10.1093/nargab/lqaf071
Standard Article

OXFORD

The divergent intron-containing actin in sponge morphogenetic processes

Yulia V. Lyupina[1,*,†], Kim I. Adameyko[1,†], Vasiliy M. Zubarev[2,†], Alexander V. Cherkasov[2], Alina V. Ryabova[3], Kirill V. Mikhailov[4,5], Sergey A. Golyshev[4], Anton V. Burakov[4], Alexander D. Finoshin[1], Pavel A. Erokhov[1], Marat S. Sabirov[1,6], Anna I. Zhurakovskaya[1], Rustam H. Ziganshin[7], Nikolai G. Gornostaev[1], Vasilina M. Ignatyuk[1], Aleksei M. Kulikov[1], Victor S. Mikhailov[1], Guzel R. Gazizova[3], Elena I. Shagimardanova[2,6], Oleg A. Gusev[8,6], Ekaterina E. Khrameeva[2], Oksana I. Kravchuk[1]

[1]N.K. Koltsov Institute of Developmental Biology, Russian Academy of Sciences, 119334 Moscow, Russia
[2]Skolkovo Institute of Science and Technology (Skoltech), Center for Molecular and Cellular Biology, 121205 Moscow, Russia
[3]Research center "Regulatory genomics", Institute of Fundamental Medicine and Biology, Kazan Federal University, 420111 Kazan, Russia
[4]A.N. Belozersky Institute of Physical and Chemical Biology, Lomonosov Moscow State University, 119234 Moscow, Russia
[5]A.A. Kharkevich Institute for Information Transmission Problems, Russian Academy of Sciences, 127051 Moscow, Russia
[6]Life Improvement by Future Technologies Institute, 121205 Moscow, Russian Federation
[7]Shemyakin and Ovchinnikov Institute of Bioorganic Chemistry of the Russian Academy of Sciences, 117997 Moscow, Russia
[8]Department of Regulatory Transcriptomics for Medical Genetic Diagnostics, Graduate School of Medical Sciences, Juntendo University, Tokyo 113-8421, Japan

[*]To whom correspondence should be addressed. Email: ylyupina@idbras.ru
[†]Yulia V. Lyupina, Kim I. Adameyko, and Vasiliy M. Zubarev contributed equally to this work.

Abstract

The ability of eukaryotic cells to orchestrate mechanical interactions from the subcellular to the organismal levels is mediated by their cytoskeleton. One of the key components of the eukaryotic cytoskeleton is actin, a highly conserved building block of the actin filaments, which interact with many other proteins and underlie diverse cell structures, necessary for organizing intracellular transport, phagocytosis and cell movement. Many organisms have evolved multiple actin variants, which share similar amino acid sequences but differ more dramatically at the gene level, including the presence and number of introns. In the current study, we show that the intron-containing and intronless actin genes are present in the poriferan *Halisarca dujardini* and that the encoded actins can perform different functions. These actins differ in the gene expression profiles, post-translational modifications, cellular, and subcellular localizations. The intronless actin genes of *H. dujardini*, *HdA1/2/3*, are products of recent duplications, exhibit low divergence between paralogs, and serve as the primary cytoskeletal actins. The divergent intron-containing actin gene, *HdA6*, is differentially expressed in a specific cell lineage and its expression is dependent on the state of cell aggregation, which indicates its unique functions in the morphogenetic processes of the sponge.

Introduction

The evolutionary development of multicellularity is inextricably linked with the processes of cell adhesion and cooperation. Re-aggregation of separate cells has retained key importance in the embryonic development and regeneration in Metazoa. Assembly of a functional organism from a suspension of dissociated cells does not normally occur in animals *in vivo*, but some metazoans do possess this remarkable ability [1, 2]. The sponges (Porifera) are an evolutionarily ancient phylum of multicellular organisms that can regenerate juvenile-like individuals from dissociated cells [3], and the rate of cell reaggregation varies among the sponge species and depends on the sponge reproduction period [4–6]. The sponge body does not contain well-defined tissues, but it comprises various cell types characterized by distinct structures, functions, or unique expression profiles [7]. The Cnidaria (e.g. hydras), Platyhelminthes (e.g. planarians), and Tunicata (e.g. ascidians) are more complex organisms with tissues, yet they also display a remarkable ability to regenerate tissues or whole organisms from some types of dissociated cells [8, 9]. Interestingly, dissociated embryonic cells of *Danio rerio*, *Triturus alpestris*, and *Xenopus leavis* can aggregate and reorganize into structures resembling early embryonic stages [10–12]. The re-aggregation and self-organization of dissociated mammalian stem and embryonic cells are fundamental in the *de novo* reconstruction of organoids from cell suspensions by tissue engineering techniques [13–15]. Mechanical signals for cell communication, perception, and response, mediated by their cytoskeleton, are regulated in space and time, ensuring the integrity of the organism during periods of growth,

Received: November 13, 2024. **Revised:** March 6, 2025. **Editorial Decision:** May 12, 2025. **Accepted:** May 16, 2025

development, and reproduction. The key component of the cytoskeleton is actin, a biopolymer, playing a pivotal role in these processes. Diversity and adaptability of actin-based mechanisms underscore their significance in both unicellular and multicellular states [16]. Actin was first isolated from mammalian skeletal muscle and named as α-actin because of its involvement in myosin contraction (activation) [17, 18]. Further studies revealed other actins in mammalian cells, which were named β- and γ-isoforms of actin, correspondently. Sequencing have confirmed six different actin genes in mammals, each encodes one protein: $\alpha_{skeletal}$-actin, $\alpha_{cardiac}$-actin, α_{smooth}-actin, γ_{smooth}-actin, β_{cyto}-actin, and γ_{cyto}-actin. Actin as a single copy gene occurs in yeast, but actin isoforms are present as multigene families in protists, plants, and animals [19]. Heterologous actin variants specialized in assembling various networks enable the cytoskeleton to respond dynamically to external influences, preserving cell viability [20, 21]. The expression of actin isoforms at the protein level in mammals is tissue-specific. Non-muscle mammalian cells express β- and γ-actin, which are almost identical (99%), but are localized in different cellular compartments [22–25]. Disturbance in the expression of β-actin gene causes embryonic death in mice, while γ-actin expression disturbances are not lethal [26, 27]. It is believed that there is a code in the structure of actin genes that controls the functional diversity of actin isoforms [28]. The eukaryotic actins share very similar amino acid sequences and differ at the nucleotide level, especially in their exon/intron organization. Most genes encoding actins have introns, but intronless actin genes also appear in the evolutionarily distant animals [29–31]. The β-actin encoding gene is regulated by several *cis*-acting regulatory elements including the evolutionarily conserved CC $(A/T)_6$GG (serum-response element (SRE) or CArG box) sequences positioned in the promoter region between the CAAT and TATA boxes [32, 33]. The proximal CArG motif is required for actin expression in developing animals, and interactions between the promoter and intron CArG motifs are important for its regulation [34]. Actin has the ability to transition between monomeric (G-actin) and filamentous (F-actin) states under the control of adenosine triphosphate (ATP) hydrolysis, presence of ions, and various actin-binding proteins. Nuclear actin is represented predominantly by G-actin monomers, but it forms F-actin filaments in reprogrammed or stimulated cells [35–37]. The motile cells, as well as cells with increased adhesive properties, differ by the level of reactive oxygen species (ROS) and the state of actin polymerization [38, 39]. All actin isoforms undergo *N*-terminal processing and post-translational modifications (PTMs) affecting their biochemical and functional properties [40]. Actin filaments can promote the formation of cellular protrusions that allow cells to migrate toward each other and establish stable contacts. Moreover, actin interacts with various proteins, including cell adhesion molecules (CAMs) and extracellular matrix (ECM) components, to modulate cell-to-cell interactions. These actin-dependent processes are important in coordinating cell behavior during re-aggregation. Cells of the same type may use different movement modes mediated by the coordinated activity of actin-associated proteins and RhoA-signaling and Hippo/YAP-signaling pathways [41–47] and can be modulated by the Merlin protein [48], as well as Rho-GTPases [49, 50]. Interestingly, macrolides (latrunculin A and jasplakinolide) that have been isolated from some marine sponges inhibit actin depolymerization, causing cell lethality in a wide range of organisms [51–53]. Information on the structural and functional features of actin in basal animals remains limited. Studying actin in cell re-aggregation of sponges provides deep insights into the fundamental principles governing tissue formation and regeneration.

The sponges are filtrators, and their aquiferous system undergoes numerous rearrangements throughout the life cycle and in response to environmental changes [54, 55]. Redox and metabolic cycle phases stimulate sponge cell movement and transformation, allowing some cells to transition between multiple cell types [6, 56, 57]. Sponge cell movements are similar to amoeboid ones and are carried out via the actin dynamics [58]. In order to migrate within the sponge body, cells must be able to invade and adhere to the mesohyl (sponge ECM with embedded collagen fibers, various cell types, and symbiotic microbial community), and perform chemotaxis—all of which are enabled by rapid actin cytoskeleton reorganization. Colgren & Nichols, studying the aquifer system of the juvenile freshwater sponge *Ephydatia muelleri*, found that its contractile module consists of myosin II and transgelin, regulated by Ca^{2+} ions and biochemical pathways involving myosin light chain kinase (MyHC II) and myocardin-related transcription factor (MRTF) [59]. In addition, sponges coexist with algae and symbiotic microorganisms, with some intracellular symbionts shown to persist through reproduction and be crucial for sponge survival [60]. Internal cytoskeletal architecture likely ensures the coexistence of sponge cells and symbionts since the eukaryotic actin is a target for uptake and disposal by pathogens [61, 62]. Recent data indicate that the axial filament formed by actin initiates and defines the zones of biomineralization, while actin elongation and branching determine the shapes and sizes of sponge spicules [63]. Intertidal sea sponges are unique models for studying cellular plasticity, as they experience daily mechanical stress from tidal waves, along with seasonal fluctuations in oxygenation and salinity. Previously, we identified iron-metabolic pathways associated with the cell reaggregation in the cold-water sea sponge *Halisarca dujardini* [64, 65] and demonstrated that cytoplasmic microtubule networks arise during activation of sponge cell transdifferentiation processes [58]. It is still unclear whether the cytoskeleton is rearranged in a cell type-specific manner during reaggregation of sponge cells after mechanical dissociation of the sponge body. The aim of this article is to explore the multifaceted roles of actin during morphogenetic processes of cold seawater sponge *H. dujardini*. The actin genes of sponges *H. dujardini* and *Halichondria panicea* (cl. Demospongia) were recovered and their structures were determined. To identify the features of signaling pathways that promote cytoskeleton remodeling during sponge cell reaggregation, the expression of actin and actin-related proteins (ARPs), tubulins, and RhoA-signaling and Hippo/YAP signaling pathways of sponge *H. dujardini* was assessed using RNAseq of the intact body, dissociated cells and cell aggregates of sponges collected during different seasons, and, accordingly, in different periods of its annual reproduction cycle. The single cell RNAseq was performed to find the specific cell clusters with differential expression of actin. PTMs of actin were detected in the cells of mature species and larvae, as well as in different cell fractions. In addition, we revealed the role of actin dynamics in morphogenetic processes of the sponge by using a specific inhibitor of actin depolymerization jasplakinolide. The expression patterns of fibrillar actin in sponge body cells, dissociated cells, and cell aggregates, as well as in sponge larval cells, were assessed using immunofluorescent labeling of

fibrillar actin and linked to the functional state of the cells. By unraveling the complexities of actin dynamics during sponge cell re-aggregation, we can better understand the remarkable regenerative capacities of some metazoans and potentially exploit these mechanisms for human.

Materials and methods

Specimen collection

Specimens of the two cold-water sea sponges *Halichondria panicea* and *H. dujardini* (cl. Demospongia) were collected at the White sea subtidal zone near the N.A. Pertsov White Sea Biological Station of Lomonosov Moscow State University (66°340 N 33°080 E) as described earlier [64]. No specific permissions were required for sampling according to the local guidelines.

Sponge body dissociation/reaggregation procedures and live imaging

The dissociation/reaggregation experiments were carried out with *H. dujardini* in different periods of its life cycle [66], as described earlier [64].

Imaging of live sponge cells was performed by Zeiss LSM880 confocal microscope, equipped with Zeiss Plan-APOCHROMAT 63x/1.4 Oil DIC objective lens (Zeiss, Oberkochen, Germany) combined with the Okolab system for temperature control of the experimental dish with cells, as described previously [58].

ROS were detected using 2′,7′-dichlorodihydrofluorescein diacetate (H_2DCFDA, "Lumiprobe," Russia) in living cells immediately after sponge body dissociation at +6 +8°C. The sponge was incubated with H_2DCFDA (1 μM) for 30 min before dissociation. ROS were recorded by the live cell imaging with confocal laser scanning microscope Carl Zeiss LSM 880. The excitation and emission parameters were 511 and 533 nm, respectively.

Jasplakinolide at doses of 1–4 μM, or vehicle, was added into the incubation medium (filtered sea water, FSW) to find out whether actin depolymerization affects *H. dujardini* cell movement and re-aggregation.

Genomic analyses

Genomic features analysis

The data from our previously published transcriptomes for *H. dujardini* and *H. panicea* (NCBI project numbers PRJNA594150 and PRJNA594151) were combined with the draft genome of *H. dujardini* [65] and the recently published genome of *H. panicea* (GCF_963675165.1). We searched core promoter elements and the most extensively characterized upstream DNA regulatory elements of metazoan actins [32, 67–71] and CpG islands. The CpG islands were detected using the Cpgplot program of the EMBOSS suite v. 6.5.7 [72] (detailed references are listed in Supplementary Table S1).

Phylogenetic analysis of actin sequences

The dataset for the phylogenetic analysis of actins and ARPs was prepared using the orthology inference of OrthoFinder [73]. The orthogroups containing actin homologs were merged, and the sequences were aligned using MAFFT 7.525 [74] with the L-INS-i algorithm. For phylogenetic inference the alignment was processed with trimAl 1.5 [75] to remove regions with over 90% gaps. The tree reconstruction was conducted using the Bayesian inference approach of PhyloBayes-MPI 1.9 [76] employing the site-heterogeneous model LG-CAT-G4. Four independent chains were run for 20 000 cycles each, and summarized with a 10% burn-in. The consensus tree was visualized and examined using the MEGA software [77] and the iTOL v7 online tool [78]. The Ka and Ks values were estimated using the KaKs_Calculator 2.0 and the model averaging method. The nucleotide alignments of actin gene sequences were generated using the TranslatorX program [79] employing MAFFT with the L-INS-i algorithm for the guiding amino acid alignment. Identity scores between the actin sequences were computed using the Sequence Identities and Similarities online tool: http://imed.med.ucm.es/Tools/sias.html.

Transcriptomic analyses

RNA isolation, cDNA library construction and bulk RNA sequencing

The bulk RNA sequencing for *H. dujardinii* samples collected in Spring (NCBI Bioproject ID: PRJNA594150, Biosamples SAMN43567536, SAMN43567537, SAMN43567538) was performed as described previously [64] and added to the dataset containing previously sequenced samples from Summer, Autumn, and Winter seasons (NCBI Bioproject ID: PRJNA594150).

Single cell RNA sequencing

For scRNA sequencing, two individuals of the cold-water sea sponge *H. dujardini* were collected at the end of august 2021 (Supplementary Fig. S1). We verified their osculum filtration functionality and then placed the specimen in a 50 ml Falcon tube filled with FSW and then dissociated by homogenization in a 5 ml Dounce homogenizer (Cat #D9063, Kimble) with 10 strokes using a loose pestle followed by 10 strokes with a tight pestle. To obtain a single-cell suspension, the homogenate was passed through a syringe with an 18G needle diameter. Then, the suspension was centrifuged (5 min, 1000 g, +4°C), and the pellet was resuspended in 1 ml of FSW with 0.5% BSA. Cells were passed through a 40 μm mesh filter and collected in a low-bind 1.5 ml Eppendorf tube. Cells were washed twice by centrifuging at 1000 g followed by resuspension in a small volume of FSW. Cell count and viability were assessed using trypan blue and automated cell counter (TC20, Cat #1 450 102, Bio-Rad) and the cell concentration was adjusted to 2000 cells/μl.

Cells isolated from sponges were encapsulated in droplet emulsions using a Chromium Single-Cell instrument (10x Genomics), and libraries were prepared with the 10x Genomics Chromium Controller and Chromium Single Cell 3′ Kit v3 (Cat #PN-1000121, 10x Genomics, USA). cDNA synthesis and library construction were performed according to the manufacturer's recommendations. Single-cell libraries were sequenced on an Illumina HiSeq 2500 using the following read parameters: 26 cycles for Read 1 (cell barcode and UMI), 8 cycles for the i7 sample index, and 98 cycles for Read 2 (transcript). Raw scRNA-seq data were deposited in the NCBI SRA database under BioSamples SAMN42483027 and SAMN42483028. Single-cell RNA-seq reads were aligned to the reference genome with CellRanger v6.1.2. [80]. The mitochondrial genome from [81] was added to the reference. To improve the fraction of successfully aligned reads, we used the first alignment attempt to extend the 3′-UTR annota-

tions with peaks2utr [82] and then realigned all reads. Read count normalization, variable feature selection, scaling, and dimension reduction were initially performed independently for each replicate using Seurat v.5 (for details see Supplementary Text) The SAMap algorithm [83] was used to compare the obtained *H. dujardini* cell clusters with the cell types from scRNA-seq dataset of other sponges (*Spongilla lacustris* [7] and *Amphimedon queenslandica* [84]).

To trace the dynamics of cell types by re-aggregation stages, the scRNA-seq and bulk was integrated with RNA-seq datasets. Bulk RNA-seq reads were aligned to the reference genome and read counts were calculated using STAR [85]. To estimate cell type proportions in bulk RNA-seq samples, cell type deconvolution was performed using MuSiC [86]. In this analysis, clusters 0 and 2 were combined into the 'cluster0 + 2' category due to their similar expression patterns, which made the predicted proportions of cluster0 and cluster2 cells unstable and highly dependent on the gene set used in the deconvolution analysis. Clusters 19 and 20 were excluded due to the small number of reliable marker genes. To obtain a single prediction for each combination of factors (Season and Reaggregation stage) a mixed linear model was built with the lme4 R package [87] using the following formula:

$$MusicEst = CT : Stage + (1|CT : Season),$$

where MusicEst is a MuSiC cell type abundancy prediction, CT is cell type, Season is one of four seasons, and Stage is one of three reaggregation stages. Focusing on the effect of reaggregation stage, it was treated as a fixed effect, while Season is a random effect. We believe that the reaggregation stage has some effect independent of the season. The Season and Stage were considered as factors nested within Cell type to allow Season and Stage to have different effects on different cell types. It is worth noting that MuSiC results are constrained such that the sum of all cluster abundances is 1, whereas such a condition cannot be imposed artificially on the mixed linear model. Though the sum of all predictions for a given season/stage combination remains close to 1.

Bulk RNA-seq differential expression analysis

Single-end reads from samples collected at four time points over an annual cycle (Winter, Spring, Summer, and Autumn) and from three re-aggregation stages (sponge body, a cell suspension 30 min after dissociation, and cell aggregates 24 h after dissociation) were mapped to the genomic assembly using STAR v.2.7.11 [85]. Read counts were quantified with featureCounts v.2.14.2 [88] using the parameters "-s 2 -M –fraction." Differential expression was then analyzed using the R package edgeR v.3.42.4 [89] by fitting a GLM Quasi-Likelihood model with the contrasts "cell suspension – intact body" and "cell aggregates – intact body" for each season. *P*-values from all contrasts were pooled and adjusted collectively using the Benjamini–Hochberg procedure to control the overall false discovery rate. The DE thresholds were set at FDR = 0.001 and an absolute fold change of 1.5. Finally, curated gene sets were visualized using the R package ComplexHeatmap v.2.7.7 [90].

RACE analysis

Full-length *H. dujardini* HdA1/2/3 cDNA flanked by adapter sequences was obtained using the Mint technology with the Mint RACE cDNA amplification set (Eurogen, Moscow, Russia) [91]. The first cDNA strand was amplified by Step-Out PCR [92] using a specific primer and the Step-Out primer mix kit (Eurogen, Moscow, Russia). The resulting PCR products were cloned into the pAL2-T plasmid (Eurogen, Moscow, Russia) and sequenced.

mRNA fluorescence *in situ* hybridization of *H. dujardini* cells

H. dujardini cells or body tissue on coverslips were fixed at 10°C in 4% paraformaldehyde in FSW for 20 min (for cells) or 1 h (for body tissue). Specimens were washed in phosphate-buffered saline (PBS), dehydrated and stored in 50% ethanol. The specimens were brought to room temperature (RT) and rehydrated through serial dilution in PBS. For *H. dujardini actin* isoform labeling, single-stranded DNA oligos labeled with Cy3 or Cy5 were used (Supplementary Fig. S2). Each *actin* isoform was detected using at least two oligonucleotide probes, one of which was isoform-specific, containing a sequence of 30–35 nucleotides complementary to the mRNA of *HdA1/2/3*, *HdA6*, or *HdA7* (Supplementary Fig. S2, for details see Supplementary Text). Images were acquired with a Zeiss LSM 800 laser scanning confocal microscope using Airyscan technology [93]. High-precision layered images (Supplementary Fig. S3) were analyzed using the FISH-quant v3 program designed for smFISH image analysis and implemented in the MatLab R2022a platform. Comparisons between the *H. dujardini* actins were performed using ANOVA, followed by Tukey's test. The level of significance was set to 1%.

Proteomic analyses

Comparative analysis of sponge actin sequences

Amino acid sequences of invertebrate and human actins were downloaded from the NCBI protein database. Additional sponge genomic and transcriptomic assemblies (listed in [65]) were screened for actin sequences using blastp from the NCBI BLAST + package v2.13.0+ [94] and exonerate v2.4.0 [95]. Domain architecture and similarity with human β-actin were assessed using InterPro v.99.0 [96], the CD-search against the CDD v.3.21 database [97], and the Needle global alignment tool from the EMBOSS suite v.6.5.7 [72]. Partial, low-quality, and prokaryotic sequences, as well as centractins and other ARPs, were removed. Unannotated sequences with less than 70% identity to the human β-actin were designated as "actin-like." The sequences were aligned using Clustal Omega v.1.2.4 [98] with default settings and visualized alongside the secondary structure of human β-actin (PDB ID: 6NBW) using the ESPript web-server v.3.0 [99] and Jalview v.2.11.2 [100]. The list of functional and inhibitor-binding residues of the human β-actin was obtained from literature [101–103], while the heme-binding residues were predicted using the HeMoQuest web-server [104].

Protein structure modeling

The 3D structures of *H. dujardini* and *H. panicea* actins were modeled using the SWISS-MODEL web server [105] and the AlphaFold v.3.0 web server [106], and visualized with PyMol v2.5.2 [107]. Template structures on the SWISS-MODEL server were selected based on Global Model Quality Estimate scores, with the *Acanthamoeba* actin structure (PDB: 4EFH) used for *H. dujardini* actins 1, 2, 3, and *H. panicea* actin models, and the *Caenorhabditis elegans* actin structure (PDB: 1D4X) used for the *H. dujardini* actin 6 model.

Nuclei isolation for electrophoresis and western blotting

The tissue was incubated in 150 μL of Buffer 1 (25 mM Tris-HCl pH 7.4, 1 mM $MgCl_2$, 5 mM KCl, 1 mM DTT, 1% NP-40, protease inhibitor cocktail) for 15 min at 4°C and vortexed to mix and then centrifuged at 3000 rpm for 5 min at 4°C. The supernatant, containing the cytoplasmic fraction, was collected. The pellet was resuspended in 1 mL of Buffer 2 (25 mM Tris-HCl pH 7.4, 1 mM $MgCl_2$, 5 mM KCl, 0.3 M sucrose, protease inhibitor) and was centrifuged at 6000 rpm for 5 min at 4°C. Around 50–70 μL of Buffer 3 (20 mM Tris-HCl pH 7.4, 400 mM NaCl, 1.5 mM $MgCl_2$, 0.1% NP-40, 1 mM DTT, protease inhibitor cocktail) was added to the pellet. The tube was shaken for 30 min in a cold room and centrifuged at 10 000 rpm for 5 min. The supernatant, containing the nuclear fraction, was transferred to a new tube.

Isolation of granulated cells for TEM, electrophoresis, and Western blotting

To isolate cells with granules from the sponge body tissue, the cell suspension was fractionated using a Percoll gradient with cutoffs of 30%, 70%, and 90%. Cells with granules were concentrated at the 30%/70% boundary of the Percoll gradient (Supplementary Fig. S4A). The isolated cells were pooled in 1000 mL of FSW, centrifuged at 300 rpm, and washed three times with FSW. Cells with granules confirmed by transmission electron microscopy (TEM) (Supplementary Fig. S4B) were used for proteomic analysis.

TEM of sponge body tissue and granulated cells

For the ultrastructural studies, the sponge body tissues and the isolated cells on the coverslips were fixed with 2.5% glutaraldehyde solution in FSW for 24 h and processed as previously described [58]. Ultrathin sections with a nominal thickness of 80 nm were prepared using Reichert-Jung Ultracut E ultramicrotome equipped with a Diatome Ultra 45 diamond knife. Sections were mounted on formvar-coated copper slot grids and post-stained with lead citrate for 3 min. Specimens were studied and imaged using JEM 1400 electron microscope (JEOL) running at 80 kV and equipped with QUEMESA digital camera (OSIS).

Electrophoresis and Western blotting

The ferritin complex band was isolated from the native gel as described earlier [65]. The *H. dujardini* body tissue, dissociated, aggregated cells, nuclear and cytoplasmic fractions, and larvae lysates were separated by sodium dodecyl sulfate-polyacrylamide gel electrophoresis (SDS-PAGE) electrophoresis as described earlier [64, 65]. The *H. dujardini* body tissue, dissociated, aggregated cells and larvae lysates containing 80 μg of protein were diluted in the sample buffer and maintained for 3 min in a water bath at 95°C. SDS-PAGE electrophoresis (160V) in 10% or 12% polyacrylamide gel was performed followed by Coomassie blue staining or protein transfer to a 0.45-μm nitrocellulose membrane. The membranes were incubated with rabbit A2066 antibody against the C-terminus of alpha actin (Sigma, Israel) or mouse ACTBD 11B7 antibody against the C-terminus of beta actin (Santa Cruz Biotechnology, Santa Cruz, USA) or rabbit pAb antibody to H3 histone (H0164, Sigma-Aldrich, USA).

LC-MS/MS analysis

Samples were loaded in buffer (2% ACN, 98% H2O, 0.1% TFA) at a flow rate of 4 mL/min into a custom-made trap column (50 × 0.1 mm) packed with Reprosil-Pur 200 C18-AQ 5 μm (Dr. Maisch) at RT, then into a home-packed fused-silica column (300 × 0.1 mm) packed with Reprosil-Pur C18-AQ 1.9 μm (Dr. Maisch) and connected to an emitter prepared with a P2000 Laser Puller (Sutter, USA). Reverse-phase chromatography was performed using an Ultimate 3000 Nano LC System (Thermo Fisher Scientific) coupled to an Orbitrap Tribrid Lumos mass spectrometer (Thermo Fisher Scientific) via a nanoelectrospray source (Thermo Fisher Scientific) (for details see Supplementary Text).

MS raw files were analyzed using PEAKS studio 10.0 (Bioinformatics Solutions Inc.) [108]. Proteins were identified by searching against the *H. dujardini* and *H. panicea* sequence databases (NCBI project numbers PRJNA594150 and PRJNA594151), with carbamidomethylation of cysteine as a fixed modification, and deamidation of asparagine/glutamine and methionine oxidation as variable modifications. False discovery rate (FDR) for peptide-spectrum matches as determined by searching a reverse database was set to 0.01. Enzyme specificity was set for cleavage at the C-terminal arginine and lysine, with a maximum of two missed cleavages allowed in the database search. Peptide identification was performed with an allowed initial precursor mass deviation of up to 10 ppm and an allowed fragment mass deviation of 0.05 Da.

Immunofluorescence assay of *H. dujardini* cells

Immunofluorescent staining with the actin antibodies and phalloidin (for F-actin) was performed for *H. dujardini* samples to assess actin distribution within the cells. The polyclonal rabbit A2066 (Sigma, Israel) or monoclonal mouse ACTBD 11B7 (Santa Cruz Biotechnology, Santa Cruz, USA) antibodies against β-Actin were used for the assessment of the subcellular localization of protein (Supplementary Fig. S5). Dissociated cells were incubated for 1 h in FSW in a six-well plate with a coverslip at the bottom to mount the cells, and then fixed with 3.5% paraformaldehyde solution (in FSW) for 15 min. To reveal actin distribution in sponge tissue, individual specimens were fixed with 3.5% paraformaldehyde solution (in FSW) for 2–6 h at RT, washed in PBS, and embedded in cryoprotectant. Freezing was carried out at −40°C in hexane. Sections with a thickness of 12 μm were cut using a Leica CM1950 cryostat and mounted onto adhesive glass slides. Sections were dried, rehydrated in PBS and stained as described [65] with the monoclonal mouse antibody against actin (1:1000) (for details see Supplementary Text).

Results

Structure of *H. dujardini* and *H. panicea* actin genes

To investigate the genetic basis of the actin plasticity in sponges *H. dujardini* and *H. panicea*, the actin genes of both sponges were identified in their genomes and their exon/intron structures were determined. We analyzed the regulatory sequences located in the promoter and more distal (enhancer) regions of the actin genes. A total of seven actin genes were identified in the genome of *H. dujardini*, along with a set of ARPs and homologs of conserved interaction partners of actin (Supplementary Table S2).

Seven actin genes in *H. dujardini (HdA 1–7)* and four in *H. panicea (HpA 1–4)* have the greatest similarity to typical cytoplasmic actins of eukaryotes (Fig. 1). Genomic data revealed that some of these actin genes are localized in proximity to each other, with some forming a tandem cluster. In *H. dujardinii*, *HdA1* and *HdA2* are located in one scaffold, while *HdA3*, *HdA4*, and *HdA7* are in another. *HpA1*, *HpA2*, and *HpA4* are positioned relatively close within a single scaffold in *H. panicea*. The colocalized actin genes of *H. dujardini*, *A. queenslandica* and two actin genes of *H. panicea* are oriented in the same direction, with individual promoters. The other two genes of *H. panicea* are on opposite DNA strands and can be regulated by a bidirectional promoter (Fig. 1). Interestingly, the intergenic distances between the pairs *HdA1-HdA2* and *HdA3-HdA4* are very similar (around 4500 bp), whereas *H. panicea* actin genes are more spread apart. The coding regions of *H. dujardini* genes *HdA1, HdA2,* and *HdA3* differ only by synonymous nucleotide substitutions. Similarly, the coding regions of *H. panicea* genes *HpA1, HpA2,* and *HpA3* displayed differences only at the nucleotide level. The coding regions of *HdA6* of *H. dujardini* and *HpA4* of *H. panicea* are markedly different from the rest of actin genes in these sponges. All four actin genes of *H. panicea* have a single intron at the position of 86 aa, while the actin gene of *A. queenslandica AqAcyt1* has an intron at the position 85 and the *AqA85C* has two introns at the positions of 75 and 85 aa. In contrast, all actin genes of *H. dujardini,* except *HdA6,* are intronless. *HdA6* has an intron at the position of 89 aa, with the length of 1043 bp – markedly longer than the actin gene introns of the other sponges (Fig. 1, Supplementary Table S3). The intron of *HdA6* contains repeating sequences (Supplementary Fig. S6), with RepeatMasker identifying four small regions (<100 nt) as repeat families, in addition to simple repeats. Each of these sections was defined as a representative of a separate unclassified repeat family constructed by RepeatModeler using the whole genome of *H. dujardini*. RepeatModeler did not reveal any full-fledged mobile elements with their own reading frames in the intron of *HdA6*. However, mirPara [109] predicted two regions that may contain miRNAs in *HdA6* (Supplementary Fig. S6).

The Inr and TATA-box are the most common elements of the actin core promoter in the studied sponges (Fig. 1). The sponge actin genes *HdA2*, *HpA2*, and *AqAcyt1* have a CArG motif without the Inr or the TATA-box. The *HdA6* and *HdA7* have only the Inr. We did not find any core promoter elements in *HpA4* of *H. panicea* and *AqAcyt1* of *A. queenslandica*. Sponge *HdA1*, *HdA5* and human *ACTB* possess CCAAT-boxes. E-box1 and E-box2 motifs were found in the sponge *HdA1, HdA3* and the human *ACTG2*. The *H. dujardini* and *H. panicea* actin genes have CpG islands of different lengths. Only *HdA1* and *HdA3*, as well as the human *ACTB* have CpG islands in the upstream regions (Fig. 1). Thus, while sponge actin genes share a similar coding sequence, their 5′ regulatory regions differ, suggesting possible independent regulation of their expression and binding with ARPs.

Next, we analyzed the diversity of *H. dujardini* actins using transcriptomes of various sponges and the human actins for comparison (Fig. 2). Comparison of the amino acid sequences of *H. dujardini* and *H. sapiens* actin isoforms revealed that HdA1/2/3 are most similar to human β-actin. HdA7 has an equal level of similarity to all human actin isoforms (Table 1, Supplementary Table S4). The isoforms HdA1/2/3, HdA4, and Hd5 differ by a few amino acids: at the positions 3, 4, and 5 in the *N*-terminal region and at the positions 54 and 307, 309, 320, and 355 (Fig. 2, Supplementary Fig. S7). The HdA6 and HdA7 differ significantly from the other actins: *H. dujardini* HdA6 experienced a surge of amino acid substitutions and shows only 74.06% identity to the conserved actin human isoforms at the amino acid level and has multiple substitutions in the functional domains, HdA7 lacks part of the *N*-terminal region, which forms the second protein subdomain (Fig. 2, Supplementary Fig. S7). It is important to note that the missing region in HdA7 carries the binding site for DNAse 1, as well as several residues involved in ATP binding (Supplementary Fig. S7). The three-dimensional structures of *H. dujardini* HdA1/2/3, HdA6 and *H. panicea* HpA1/2/3 were modeled using a published crystallographic template of actin (Fig. 3, Supplementary Fig. S8). Actin subdomains S1, S2, S3, and S4 were identified. The *N*-terminal region is located in S1 in all actins, but in HdA1/2/3 it is significantly shorter compared to the human actin (Supplementary Fig. S9).

Phylogeny of *H. dujardini* actin genes

To analyze the evolutionary history of the actin family members, we built a phylogenetic tree using the amino acid sequences of actins and ARPs, including homologs from sponges *H. dujardini*, *H. panicea*, and *A. queenslandica*. In the reconstructed phylogeny the intronless actins of *H. dujardini*, *HdA1–5* and *HdA7*, group inside a cluster of conserved cytoplasmic actins (Fig. 4). The intronless actins of *H. dujardini* form a single clade, suggesting their relatively recent origin from a single ancestral sequence through gene duplications, albeit the support values within the group of conserved actins are low. The divergent actin *HdA6* also falls within the group of conserved actins in the consensus phylogeny, but its exact position is poorly resolved and its branch is noticeably longer than that of typical actin sequences. To assess whether the divergence of *HdA6* is a consequence of gene decay due to complete loss of function, we estimated the Ka/Ks ratio among the *H. dujardini* actins. With over 300 nucleotide substitutions separating the *HdA6* from the conserved actin variants *HdA1–5*, the overall Ka/Ks ratio was estimated to be approximately 0.03, indicating strong purifying selection over the whole sequence (Supplementary Table S5). A BLAST search in the genome of *H. caerulea* (GenBank accession: GCA_963170055.1), a close relative of *H. dujardini,* did not reveal any sequences with high similarity to HdA6, suggesting that *HdA6* is a unique feature of *H. dujardini*.

Thus, the conserved *Hd1/2/3* are likely involved in fulfilling the core cytoskeletal functions of eukaryotic actins in *H. dujardini*, while the divergent *HdA6* might have acquired a separate role.

Cellular localization of *H. dujardini* actin mRNAs

To visualize the distribution of actin mRNAs in sponge cells, the fluorescence *in situ* hybridization (FISH) was used with five different oligonucleotide probes that were specifically designed to target the coding sequences of the actin genes of *H. dujardini* (Supplementary Fig. S2). The distinct localization patterns of their mRNAs in cells were revealed by using multiple combinations of oligonucleotide probes. Cells treated with *HdA1/2/3* and *HdA7* probes displayed numerous discrete spots throughout the cytoplasm, including within cellular protrusions (Fig. 5). *HdA6* mRNA was localized in

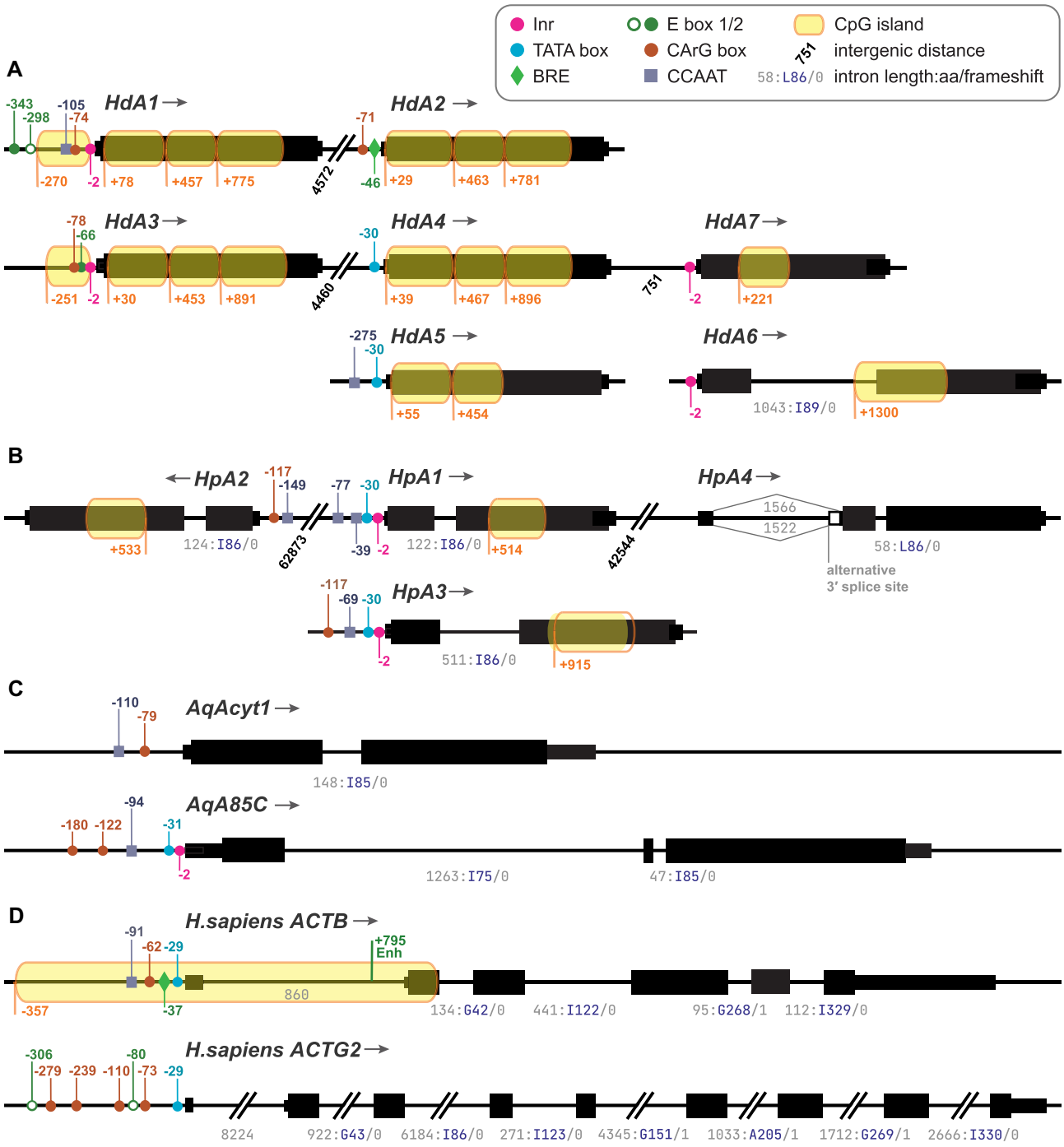

Figure 1. Regulatory elements of actin genes in sponges and humans. **(A)***H. dijardini*; (**B**) *H. panicea*; (**C**) *A. queenslandica* conservative (*AqAcyt1*) and non-conservative actin (*AqA85C)*; (**D**) human β- (*ACTB*) and γ-actin (*ACTG2*). The figure shows DNA motifs involved in gene regulation, including core promoter elements (TATA box, initiator (Inr), and transcription factor B recognition element (BRE)). Additionally, CpG islands, which can be linked to housekeeping gene expression, are present. Besides, the DNA sequences involved in the regulation of actin genes in bilateral animals, such as E-box1, E-box2, CCAAT-box, CArG-box are shown. The enhancer ATGGTAATAA, located in the intron of vertebrate actin genes, is shown for the human gene but was not found in sponges. The coordinates of the elements are indicated relative to the transcription start sites of the corresponding genes. The transcriptional start site for *HdA1, HdA2,* and *HdA3* of *H. dujardini* was identified by using RACE. For other actin genes, the start of transcription was predicted using transcriptomic data. An alternative 3'splicing site is found in the *HpA4* gene (**B**). Arrows, direction of transcription; black numbers, distances between actin genes located on the same scaffold; orange numbers, start of CpG islands; grey numbers, lengths of introns. The position in the amino acid sequence is also indicated for introns (more information about intron positions is provided in Supplementary Table S3).

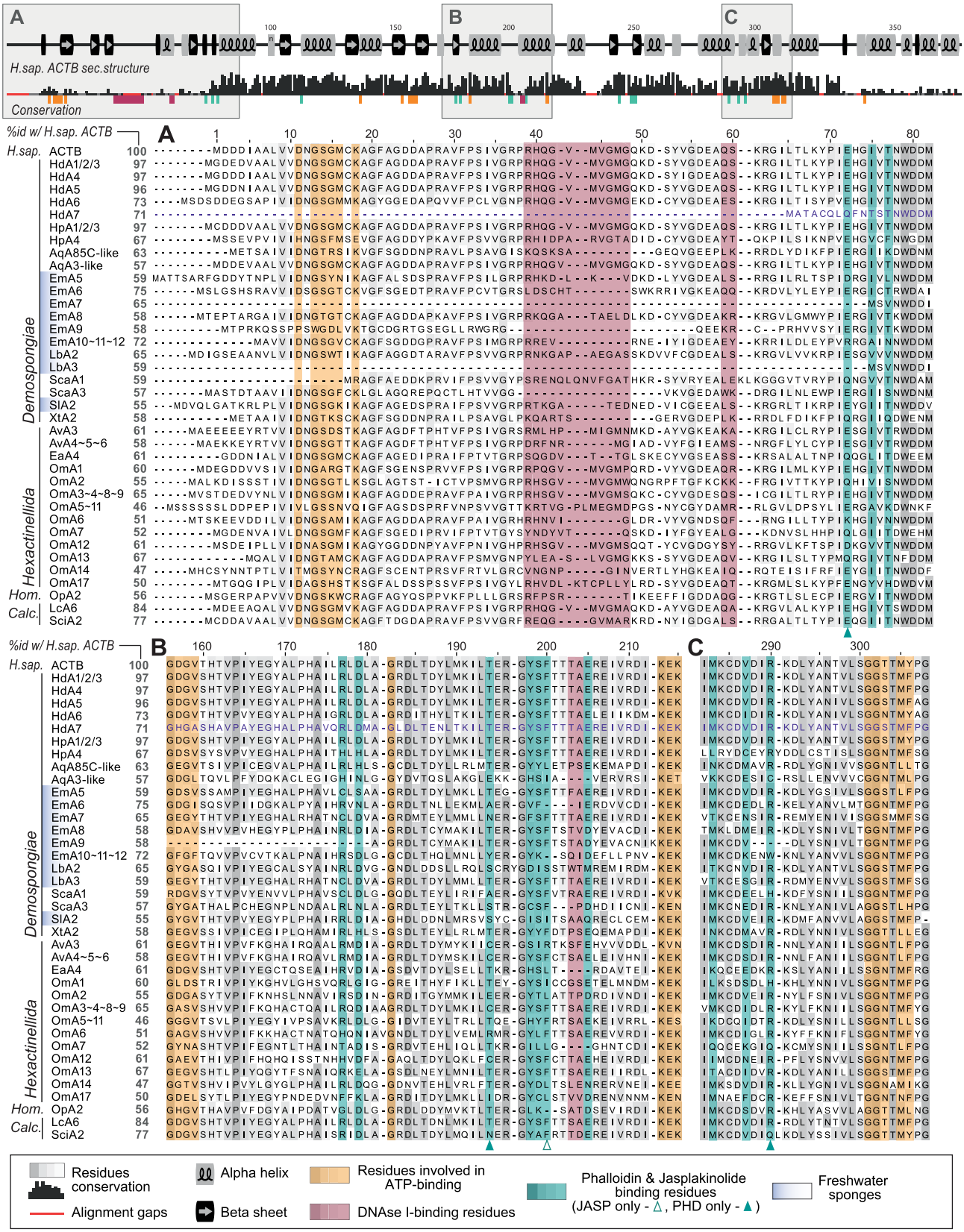

Figure 2. Functional and inhibitor-binding residues of *H. dujardini* and *H. panicea* actins aligned with non-conserved actins from other sponges and *H. sapiens* β-actin (ACTB). The top panel displays the ACTB secondary structure (PDB ID: 6NBW), alignment conservation scores, and residues involved in the ATP-binding (orange), DNAse-I binding (pink), and Phalloidin/Jasplakinolide inhibitor binding (cyan). Below, three representative regions of the alignment for selected sponge actins are shown (panels A, B, and C; accession numbers in Supplementary Table S12). Similar sequences of the same species were merged (85–99% identity denoted by "∼," 100% by "/"), showing only one representative sequence, with identity levels to human ACTB indicated next to the sequence names. *Hd, Halisarca dujardini; Hp, Halichondria panicea; Aq, Amphimedon queenslandica; Em, Ephydatia muelleri; Lb, Lubomirskia baikalensis; Sca, Stylissa carteri; Sl, Spongilla lacustris; Xt, Xestospongia testudinaria; Av, Aphrocallistes vastus; Ea, Euplectella aspergillum; Om, Oopsacas minuta; Op, Oscarella pearsei; Lc, Leucosolenia complicata; Sci, Sycon ciliatum.*

Table 1. The percent of identity between *H. dujardini* actins and *H. sapiens*

Protein name	Percent of identity with *H. sapiens* homologs (%)					
	ACTG NP_001186883.1	ACTBM Q9BYX7	ACTB NP_001092.1	ACTBL NP_001017992.1	ACTC NP_001393411.1	ACTS NP_001091.1
HdA1	96.79	89.04	97.33	90.43	93.58	92.84
HdA2	96.79	89.04	97.33	90.43	93.58	92.84
HdA3	96.79	89.04	97.33	90.43	93.58	92.84
HdA4	96.26	88.77	97.33	89.89	92.78	92.25
HdA5	95.45	87.70	96.26	89.10	92.25	91.71
HdA6	73.80	69.25	73.53	72.07	73.60	72.53
HdA7	87.87	83.95	87.87	82.95	87.96	87.29

the cytoplasm and perinuclear area, with some cells predominantly expressing *HdA6* (Fig. 5A, C). Notably, the expression of *HdA1/2/3* was significantly higher compared to *HdA6* (Supplementary Fig. S10B). Thus, the expression of the divergent actin *HdA6* is distributed across cells in more specific manner than the expression of the conserved actins, and their expression regions within cells do not overlap completely, pointing to the separation of their functions in the sponge cells.

Characteristics of protein products of *H. dujardini* actin genes

To characterize the protein products of different *H. dujardini* actin genes, homogenates from different sponge samples (body tissue, dissociated cells, cell aggregates, and larvae) were fractionated by electrophoresis in polyacrylamide gels (Supplementary Fig. S11). The proteins were extracted from the gels and processed by LC-MS/MS. The *H. dujardini* actin HdA1/2/3 has 376 amino acids, a predicted molecular weight (MW) of 41816.41 Da, and an isoelectric point (pI) of 5.15. The sequence of the truncated HdA7 isoform has only 311 amino acids, predicted MW of 34 860 Da and pI 5.3. The divergent HdA6 has 379 amino acids, predicted MW of 42038.49 Da and a pI of 4.85, which is lower than that of HdA1/2/3. Only two protein products of *H. dujardini* actin genes, along with some ARPs, were identified by LC-MS/MS (Table 2, Supplementary Fig. S12). The major HdA1/2/3 actins and the divergent HdA6 were present in the native ferritin complex and SDS-PAGE samples from body tissue, dissociated cells, cell aggregates, and larvae (Table 2). HdA6 was detected only in the nuclei of *H. dujardini* cells (Table 2). LC-MS/MS analysis revealed multiple PTMs in the HdA1/2/3 actins: acetylation, methylation, carbamidomethylation, deamidation, oxidation, and ubiquitination (Supplementary Tables S6 and S7). The GQKDSYVGDEAQSK epitope was detected in HdA1/2/3 actin (Supplementary Fig. S12). The first methionine in HdA1/2/3 was removed, and the *N*-terminus was mainly acetylated at G2, with less frequent acetylation at A19. Methylation at H73 was observed in about half of the cases, while oxidation of methionine at M16, M44, M47, and M305 occurred in approximately 75% of the observed cases (Supplementary Fig. S12). The *N*-terminus of HdA6 was not detected in the samples studied. PTMs observed in *HdA6* included methylation, carbamidomethylation, deamidation, and oxidation (Supplementary Table S6). Oxidation of methionine in Hd6 was observed at M48 and M51 (Supplementary Fig. S12). In addition, ARPs Arp2, Arp3, ARPC2, Severin/Fragmin, Profilin 1, and ERM family 2-like, which regulate actin dynamics, were identified (Supplementary Fig. S13).

To investigate the actin dynamics and distribution during morphogenic processes within *H. dujardini* sponge cells, we employed both TEM and confocal fluorescence microscopy, using antibodies specific to β-actin and phalloidin, which binds to F-actin (Fig. 6). Given the active motility and rapid changes in the shapes of sponge cells, we expected to find not only individual microfilaments but also robust bundles responsible for cellular contractility. Indeed, TEM and ultrathin section imaging revealed well-defined actin bundles spanning the cytoplasm, suggesting their role in maintaining cell structure and motility (Fig. 6A and B).

Live-cell imaging of dissociated *H. dujardini* cells showcased a variety of morphologically distinct and motile sponge cells, with different ROS status, pseudopodia sizes, and intracellular granules (Supplementary Movie 1). Time-lapse microscopy highlighted the morphological dynamics of stellate and amoebocyte-like cells, which rapidly adjusted their pseudopodia size and number during phagocytosis of bacteria or small particles (Supplementary Movie 2), as well as during cell-to-cell contacts (Supplementary Movie 3).

Confocal fluorescence imaging further elucidated the distribution of actin and F-actin-containing microfilaments in different sponge cells (Fig. 6). Cells within the sponge body tissue exhibited diverse morphological structures and varying degrees of polarization. Many cells had thin filopodia, while cells with lamellae stained with phalloidin showed actin-rich structures. Cell contacts were characterized by dot-like actin granules (Fig. 6). Morphological analysis of the anterior edges of aggregating cells after sponge body dissociation revealed various types of protrusions and distinct distributions of polymerized F-actin (Fig. 6, Supplementary Fig. S14). Some freely moving sponge cells adhered to glass surfaces and extended different projections that facilitated cell-to-cell contact and aggregation (Supplementary Fig. S14). These outgrowths, particularly in stellate and amoebocyte-like cells, as well as the lamellae, were enriched in F-actin. Cells migrating on surfaces or within the mesohyl exhibited a rounded amoeboid shape of varying sizes, with hemispherical vesicles or an actin-rich leading edge (Fig. 6). Twenty-four hours post-dissociation, the cells formed aggregates with spherical structures of varying sizes. These aggregates floated freely in the water column, contacted each other, and merged (Supplementary Movie 4), but were easily disintegrated by external influences—unlike the more stable native sponge body tissues (Fig. 7).

The mobility and direction of sponge cell outgrowths depend on F-actin turnover, which can be inhibited by

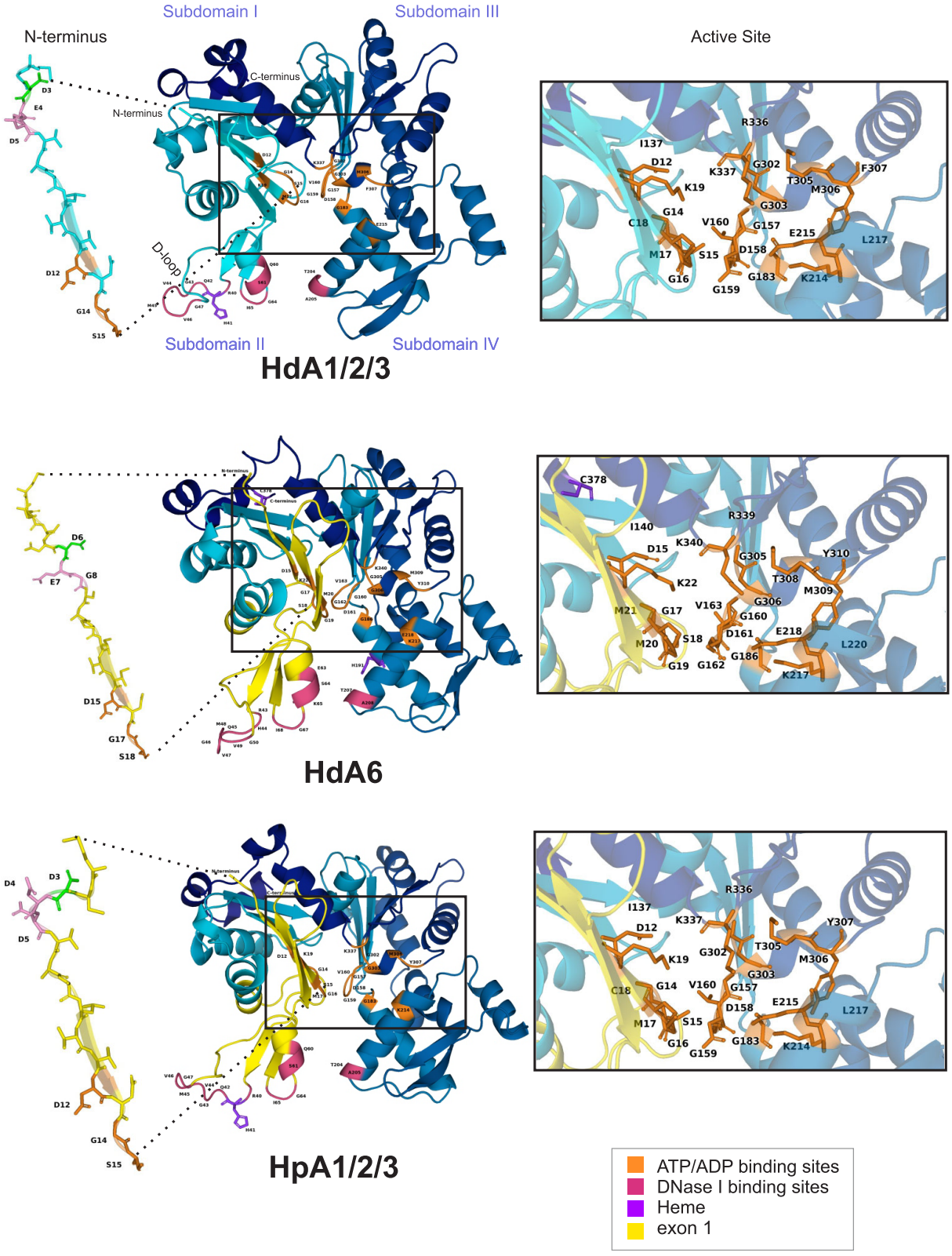

Figure 3. Predicted 3D structures of *H. dujardini* (HdA1/2/3 and HdA6) and *H. panacea* (HpA1/2/3) actins. The actin structure of *Acanthoamoeba* (PDB: 4EFH) served as a template for modeling *H. dujardini* HdA1/2/3 and *H. panicea* actins, while the structure of *C. elegans* actin (PDB: 1D4X) was used for the *H. dujardini* HdA6 model. Amino acid numbering corresponds to the human ACTB sequence, starting from the initial methionine. The *N*-terminus and active site models were predicted using the AlphaFold v3 web server, whereas the models shown in the other panels were predicted using the SWISS-MODEL server.

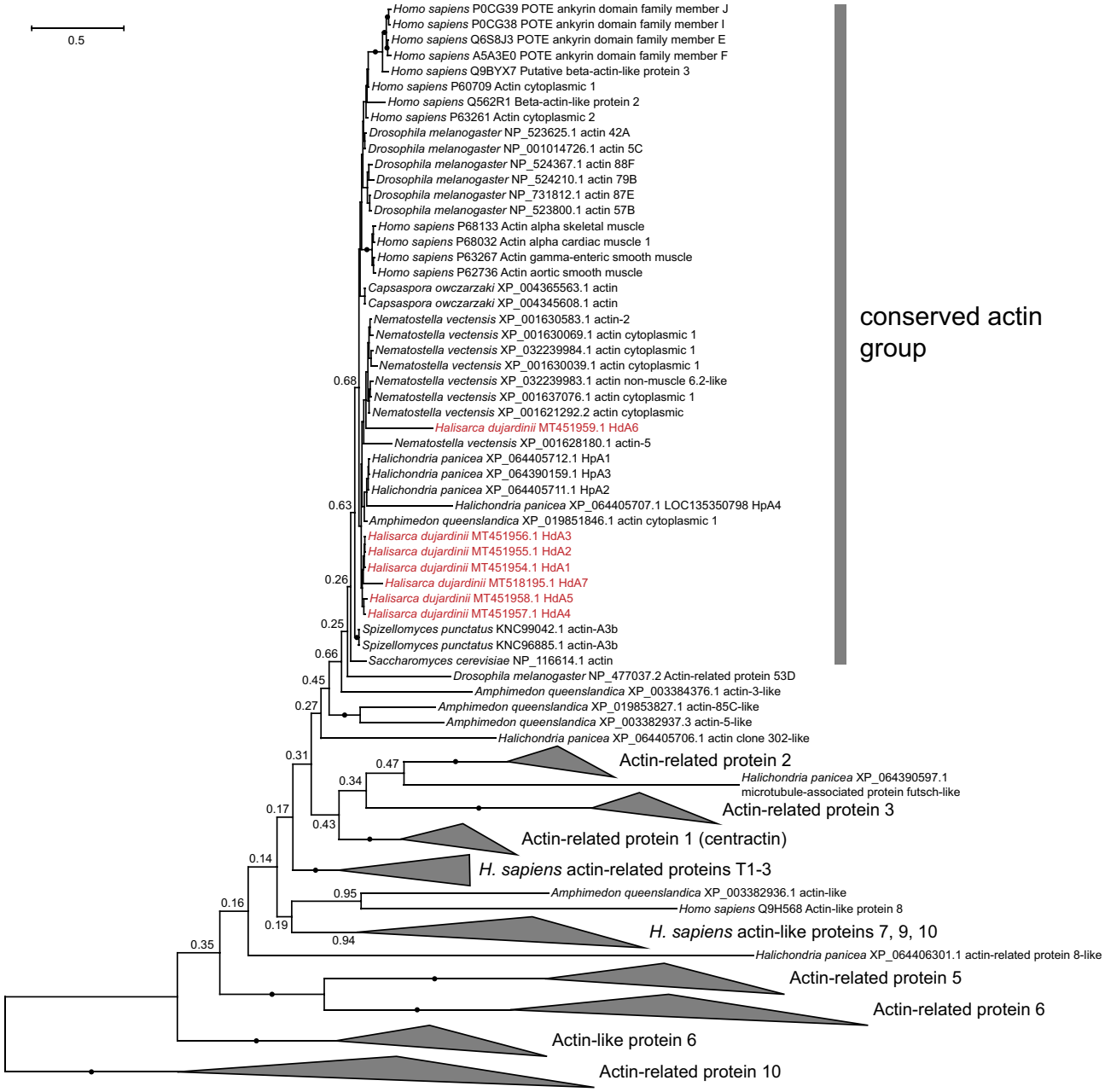

Figure 4. Phylogenetic tree of actins and ARPs. The phylogeny was reconstructed using the Bayesian inference of PhyloBayes with the LG + CAT model; branch support values are posterior probabilities estimated using four independent chains; the support values are shown for a selection of branches; black dots at the branches indicate nodes with posterior probabilities over 0.98; the sequences of *H. dujardini* are highlighted in red.

jasplakinolide, a cell-permeable macrocyclic peptide. To determine whether actin depolymerization affects *H. dujardini* cell movement and reaggregation, we used jasplakinolide to stabilize F-actin. Treatment with jasplakinolide at doses of 1–4 μM resulted in a dose-dependent decrease in the formation of small cell aggregates attached to surfaces two hours after dissociation, and it reduced the formation of spherical aggregates 24 h after sponge body dissociation (Supplementary Fig. S15). A low dose (1 μM) reduced cell movement and adhesion in dissociated cells compared to the control group 2 hours after treatment (compare Supplementary Movies 5 and 1), with most sponge body cells accumulating F-actin (Supplementary Fig. S16). However, F-actin stabilization was not observed in cells with long, thin outgrowths, marked by punctate F-actin (Supplementary Fig. S16). After treatment with jasplakinolide at 1 μM, ubiquitination of HdA1/2/3 was detected at positions K239, T280, and T328 (Supplementary Table S6).

Thus, actin in *H. dujardini* cells exhibited diverse distributions and varying degrees of polymerization throughout the reaggregation process. Newly formed elongated outgrowths were initially stained with phalloidin, indicating the presence of F-actin, followed by actin accumulation in specific compartments, eventually leading to the formation of actin granules. Stabilization of F-actin by jasplakinolide inhibited reaggregation, reduced intercellular adhesion, and altered the three-dimensional organization of cell aggregates. Actin dynamics reflect a cell-specific functional state and highlight its crucial role in cellular rearrangements, interactions, and

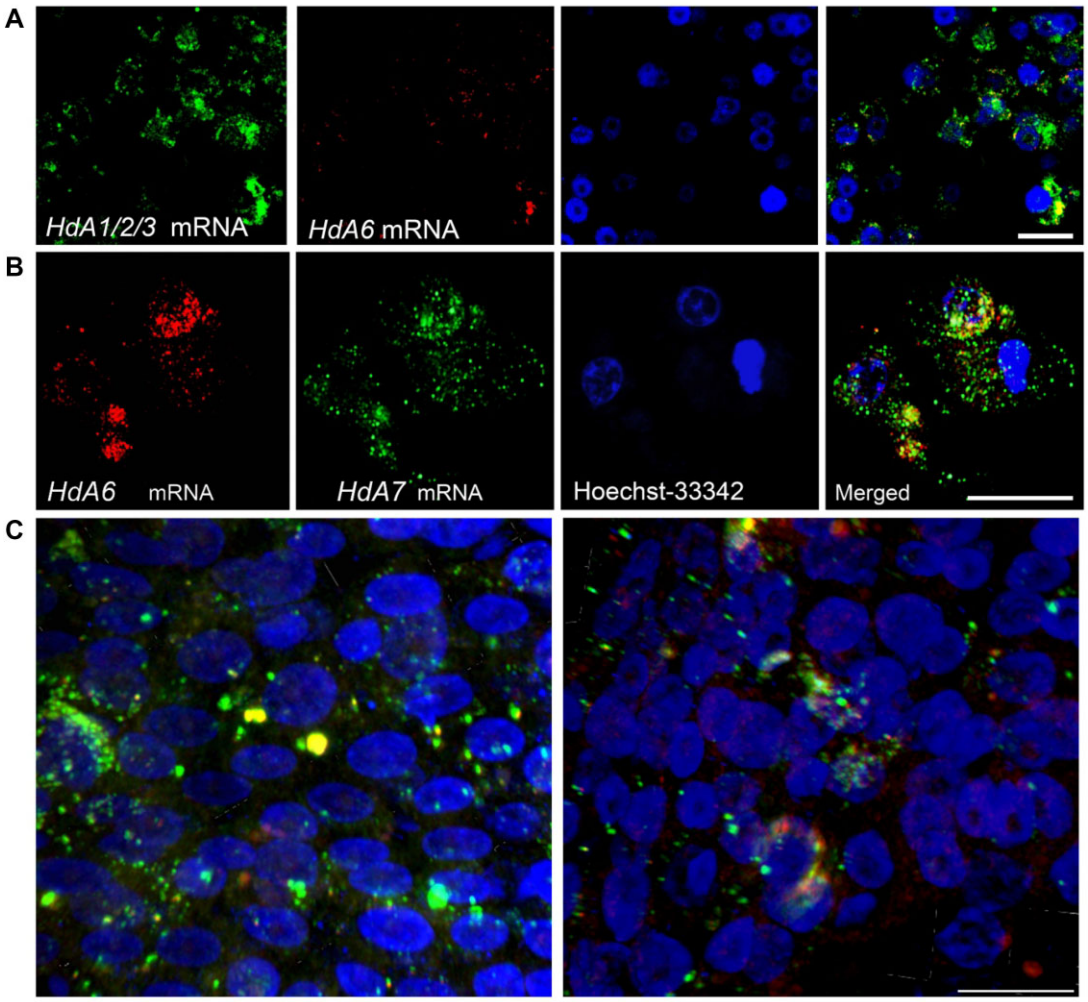

Figure 5. FISH images of mRNA distributions of *HdA1/2/3*, *HdA6* or *HdA7* in *H. dujardini* cells. The images of *H. dujardini* cells labeled by oligonucleotide probes targeting the coding sequence of the actin genes obtained with a Carl Zeiss LSM 880 confocal microscope using Airyscan technology [93]. (**A**) Confocal image of cells with oligonucleotide probes targeting the coding sequence of the actin *HdA1/2/3* (green) and *HdA6* (red); (**B**) Confocal image of cells with oligonucleotide probes targeting the coding sequence of the actin *HdA7* (green) and *HdA6* (red); (**C**). C. Representative 3D projection of body tissue cells labeled with *Hd1/2/3* (green) and *HdA6* (red) oligonucleotide probes. Nuclei were stained with Hoechst 33342. Scale bar: 10 μm.

general reorganization of sponge body tissues and during reaggregation.

H. dujardini single-cell RNA-seq experiment

In order to determine a potential role of the divergent *HdA6* in the sponge structural organization we unravel the cellular heterogeneity of *H. dujardini* and the cell-type-specific expression patterns of actin genes by the single-cell RNA sequencing (scRNA-seq) with two independent biological replicates. After applying quality control and preprocessing, expression data for 23 720 genes from 22 145 individual cells were obtained. Following initial clustering, the differential expression markers were manually inspected and cells expressing multiple or no marker sets were excluded. Reclustering resulted in 21 distinct clusters, each defined by a highly distinctive marker gene set (Fig. 8A, Supplementary Table S8A). Notably, some differentially expressed genes marked groups of clusters rather than individual clusters, suggesting a hierarchical structure within sponge cell lineages (Supplementary Fig. S17). The most abundant are clusters CL0 and CL2, both forming a large central cluster (Fig. 8A). The cluster 0 contains the largest number of cells of all the clusters in the data set and is represented by cells expressing genes for Jacalin-like protein, von Willebrand factor type A and Deleted in malignant brain tumors 1 protein-like 3, which may be actively involved in regulating the ECM and maintaining proper cellular function by inhibiting cell growth and inducing apoptosis (Supplementary Table S8A). These genes are also expressed in the cluster 2 that specifically marked by genes of histone H3 and the cell proliferation-associated Ki-67-like protein. To interpret these cell type relationships, the self-assembled manifold mapping (SAMap) [83] was applied to align the *H. dujardini* clusters with annotated cell types from the freshwater juvenile sponge *S. lacustris* [7] and the adult marine sponge *A. queenslandica* [84] (Supplementary Fig. S18). The largest cluster 0 maps to different cell types, including choanocytes and archaeocytes (Supplementary Fig. S18). The cluster 2 likely represent proliferating variants of cluster 0 cells. Interestingly, specific expression of the divergent *HdA6* was observed in clusters 3, 5, and 8 (Fig. 8B, C), which, according to SAMap analysis, corresponded to various pinacocyte subtypes and were adjacent to its main representative, cluster 1 (Supplementary Fig. S18). In contrast, other actin forms, including *HdA1/2/3*,

Table 2. Extended LC-MS/MS data-summary and supporting peptides

#	Description	Protein	-10lgP	Cov. (%)	#Peptides	#Unique	PTM	Avg. Mass
1	Body tissue	HdA1/2/3	383.99	87	683	5	Carbamidomethylation; Oxidation (M); Acetylation (Protein *N*-term); Ubiquitin	41 817
		HdA6	208.06	32	17	11	Carbamidomethylation; Oxidation (M)	42 039
2	Dissociated cells	HdA1/2/3	358.69	84	144	22	Carbamidomethylation; Oxidation (M); Acetylation (Protein *N*-term); Ubiquitin	41 817
3	Cell aggregates	HdA1/2/3	315.22	80	104	99	Carbamidomethylation; Oxidation (M); Acetylation (Protein *N*-term); Ubiquitin	41 817
		HdA6	175.71	28	14	9	Carbamidomethylation; Oxidation (M)	42 039
4	Granulated cells	HdA1/2/3		80	83	14	Oxidation (M); Deamidation (NQ); Carbamidomethylation; Acetylation (Protein *N*-term)	41 817
		HdA6		36	14	11	Oxidation (M)	42 039
5	Body tissue, Cytoplasm	HdA1/2/3	186.08	58	28	11	Oxidation (M); Deamidation (NQ); Carbamidomethylation; Acetylation (Protein *N*-term); Ubiquitin	41 817
6	Body tissue, Nuclei	HdA1/2/3	292.32	69	81	2	Oxidation (M); Deamidation (NQ); Carbamidomethylation; Acetylation (Protein *N*-term); Ubiquitin	41 817
		HdA6	106.46	18	10	8	Carbamidomethylation; Oxidation (M)	42 039
7	Dissociated cells, Cytoplasm	HdA1/2/3	224.36	44	30	15	Carbamidomethylation; Oxidation (M); Deamidation (NQ); Acetylation (Protein *N*-term);	41 817
8	Larva tissue	HdA1/2/3	657.43	92	302	7	Carbamidomethylation; Deamidation (NQ); Methylation (KR); Oxidation (M); Ubiquitin; Ubiquitination	41 817
		HdA6	300.13	69	29	24	Carbamidomethylation; Deamidation (NQ); Methylation (KR); Oxidation (M); Ubiquitin; Ubiquitination	42 039
9	Native ferritin complex of body tissue	HdA1/2/3	208.5	51	18	8	Carbamidomethylation; Oxidation (M); Deamidation (NQ)	41 817
		HdA6	62.62	7	2	2	Oxidation (M); Carbamidomethylation	42 039

exhibited uniform expression across all clusters (Fig. 8B and C).

Among the *HdA6*-specific clusters, cluster 5 has the most ubiquitous *HdA6* expression, along with marker genes of EGFR (Epidermal growth factor receptor-like) and an uncharacterized protein, which is likely specific to *H. dujardini*. (Supplementary Table S8A; Supplementary Fig. S17). SignalP predicted a signal peptide in the uncharacterized protein, and TMHMM detected no transmembrane domains, suggesting it is likely secreted. Cluster 5 cells also express a range of genes involved in signaling and cellular adhesion, including haem peroxidase (OR460109), DBH-like monooxygenase (PQ034614.1) and neural CAM L1-like (PQ415654) genes (Supplementary Table S8B). Based on the homology with other animal peroxidases and the presence of a signal peptide, the *H. dujardini* haem peroxidase likely functions in the extracellular oxidative reactions. Additionally, the DOMON-containing DBH-like monooxygenase (PQ034614.1) is predicted to bind heme at H225 (Supplementary Table S9). Cluster 3 is marked by genes encoding a serine protease HTRA1A-like protein and short-chain collagen C4, as well as by expression of myophilin-like protein (OR460124.1) and Ras-related protein Rap-2a (PQ415652) (Supplementary Tables S8A, S8B). Cluster 8 is marked by ADP-ribosylation factor genes and expresses the transcription factor Forkhead box protein L2-like (PQ415653), which is involved in maintaining genome stability and regulating gene expression, differentiation and apoptosis (Supplementary Tables S8A and B).

Next, we identified genes coexpressed with *HdA6* in the cells of clusters 3, 5, and 8 (Supplementary Table S10). The structure-specific endonuclease subunit SLX4-like protein and protein-tyrosine phosphatase genes were consistently coexpressed with *HdA6* in these clusters. In cluster 5 cells, *HdA6* was also coexpressed with genes associated with EGFR-dependent pathways, including receptor-type tyrosine-protein phosphatase delta-like, tyrosine-protein kinase, a Frizzled homologue HduFzdE, and proteins containing fibronectin type III, PH, and tenascin-X-like 1 domains. This suggests a potential role for the divergent *HdA6* in mediating cellular signaling and structural organization.

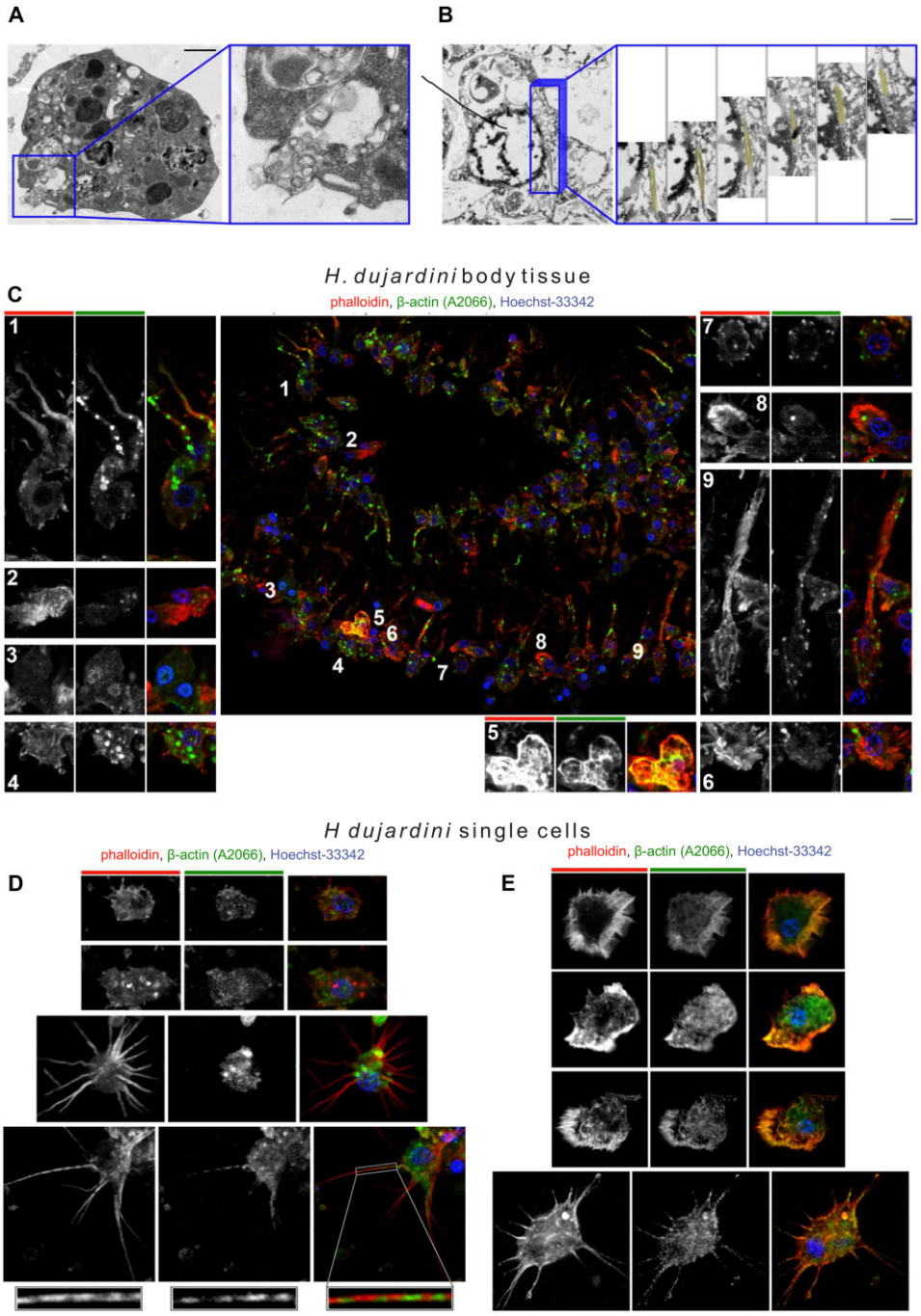

Figure 6. The actin structures and distribution in the sponge *H. dujardini* body tissue and dissociated cells. (**A**) Endo-/exocytosis captured using TEM, demonstrating active actin-dependent processes in sponge cells. The circled area is shown enlarged on the right. Scale bar: 1 μm. (**B**) TEM image demonstrating a robust bundle of actin microfilaments in the cytoplasm of a sponge cell (highlighted in yellow pseudo-color). Serial ultrathin sections from the circled area are shown enlarged on the right. Scale bar: 500 nm. (**C**) Fluorescent images demonstrating the actin distribution in *H. dujardini* body tissue. Staining with phalloidin (red) and antibody to β-actin A2066 (green), nuclei were stained with Hoechst 33 342 (blue). The cells without protrusions demonstrate pronounced stress fibrils of different sizes [2], lamellae [6], diffuse distribution of actin in the cytoplasm [3], large or small actin granules in the cytoplasm [4,7 ,8], or numerous actin bundles and transverse arches [5]. In the cells with protrusions the actin granules of various sizes were observed both in the cell soma and protrusions; stress fibrils sometimes were detected, and the phalloidin staining is more pronounced in protrusions [1,9]. (**D**) Staining of dissociated sponge cells with phalloidin (red), antibody to β-actin A2066 (green), and Hoechst 33 342 (blue). From top to bottom: non-polarized immotile cell with actin granules stained by antibodies but not phalloidin and vice versa; in the cells with protrusions the phalloidin staining prevailed in protrusions (as in C), and the β-actin antibody reveal granules in the soma (third from the top) or both in the soma and protrusions (bottom panel). In the latter case, phalloidin staining apparently disappears where antibody staining appears, without showing the slightest colocalization (circled and enlarged below). (**E**) Staining of dissociated sponge cells with phalloidin (red). antibody to β-actin ACTB 11B7 (green) and Hoechst 33 342 (blue). From top to bottom: non-polarized immotile cell demonstrates organized lamella with active ruffling, the cell moving down to the right demonstrating active blebbing, the cell moving to the left by the extension of the lamella. All three cells without protrusions have obvious co-localization of β-actin antibody staining with phalloidin in the cytoplasm periphery, i.e. in the areas of lamella extension under raffling/blebbing, and do not demonstrate colocalization in the central region. In the bottom panel, the cell with protrusions has partial colocalization of β-actin antibody staining with phalloidin and demonstrates actin granules both in the soma and protrusions.

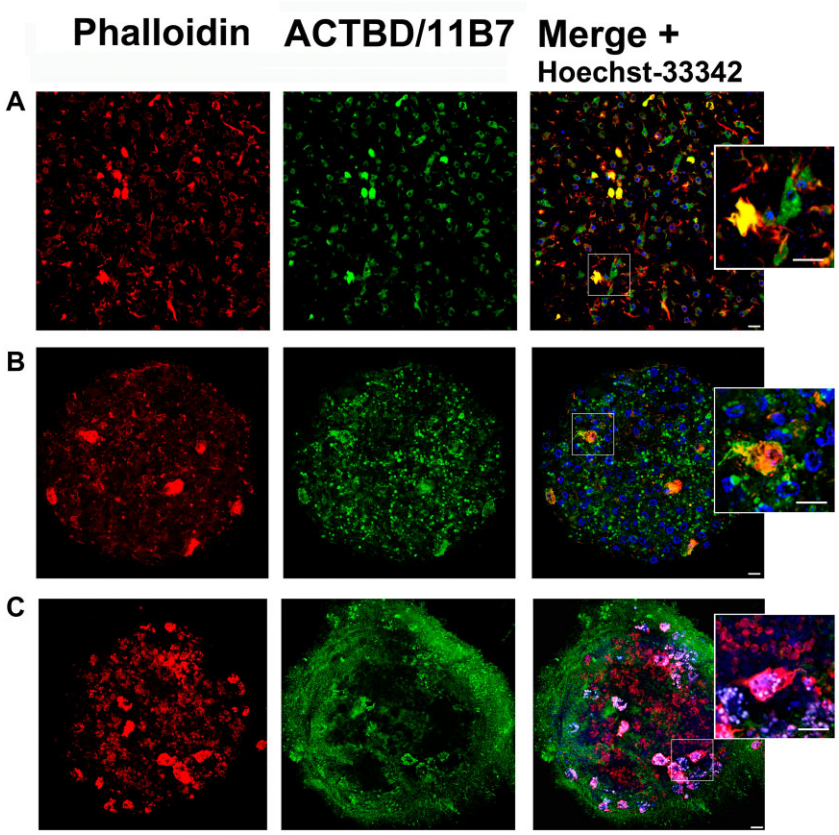

Figure 7. The distribution of actin forms in *H. dujardini* cells. Confocal images of body tissue (**A**), cell aggregates (**B**), and larva (**C**). Staining with phalloidin (red) and antibody to β-actin (green). Nuclei were stained with Hoechst 33342. Within aggregates, cells were densely packed, and some displayed long, pronounced filopodia. Immunohistochemical staining revealed a decrease of F-actin in small cells within the aggregates, and dot-like actin granules were absent in both cytoplasmic and cell contact areas (**B**). F-actin-rich cells, primarily choanoblast clusters, observed in mature sponge body and larval tissues, selected area in enlarged image **(A, C)**. Scale bar is 10 μm.

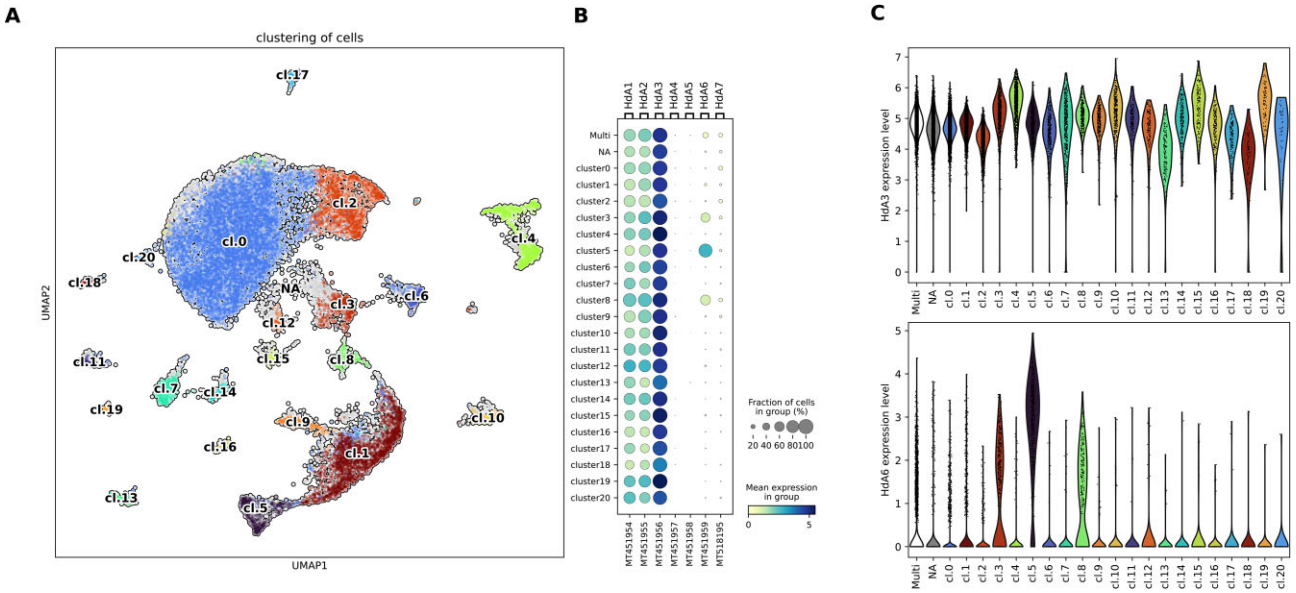

Figure 8. Single-cell RNA-seq analysis. (**A**) UMAP projection of *H. dujardini* cells after reclustering into 21 clusters, each defined by manually inspected marker gene sets (detailed in S8A Table); cells expressing multiple or no marker sets are in pale grey color. (**B**) Dotplot illustrating the expression of actin variants across single-cell clusters. Color represents the mean value of read count of the gene in particular cluster. Dot size represents fraction of cells that have non-zero level of expression of this gene. (**C**) Violin plots showing distributions of actin expression level in each single-cell cluster for *HdA3* (as a representative of the ubiquitously expressed conserved actin paralogs) and *HdA6*.

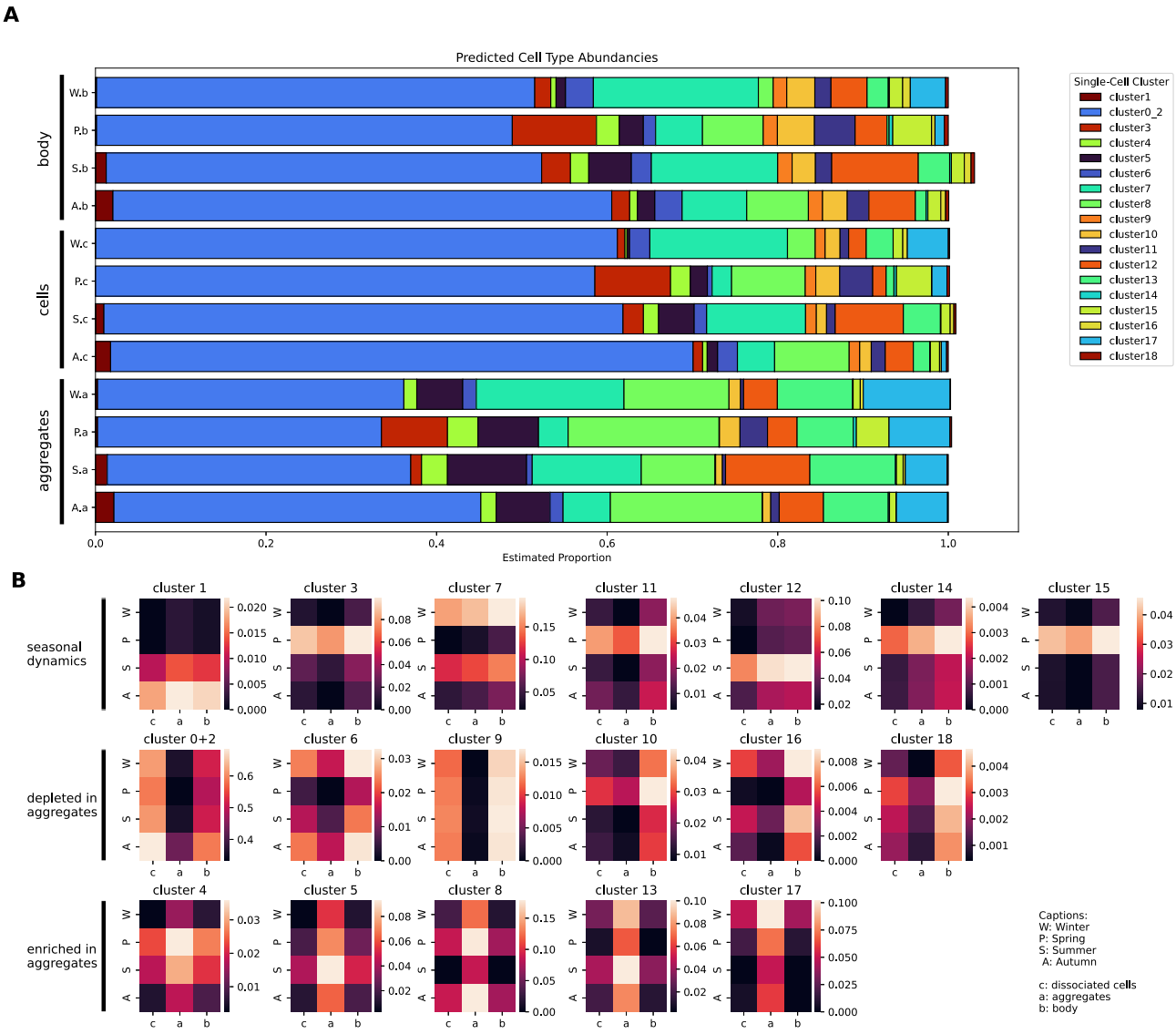

Figure 9. Cell-type deconvolution analysis. (**A**) Cell type deconvolution of bulk RNA-seq samples using MuSiC [86], with clusters 0 and 2 combined due to similar expression patterns and unstable proportion predictions, and clusters 19 and 20 excluded for insufficient marker gene stability. Results from replicates were integrated using mixed linear modeling with lme4 [87]. (**B**) Data from the same analysis in the form of separate heatmaps for each cluster helps to reveal three main patterns: only seasonal dynamics, depletion during the aggregate stage, and enrichment in the aggregate stage.

Differential gene expression and cell types dynamics during the dissociation/reaggregation process

To determine whether cellular specificity is associated with the reaggregation of sponge cells, the single-cell RNA-Seq data were integrated with bulk RNA-Seq data for sponge samples at different reaggregation states (dissociated and aggregated cells, and intact sponge body tissues). The bulk RNA-Seq dataset also captured seasonal expression dynamics, with sponge samples collected across key life cycle stages, hereafter referred to season for brevity: Winter (beginning of spermatogenesis and oogenesis), Spring (active spermatogenesis and oogenesis), Summer (onset of body tissue growth), and Autumn (end of body tissue growth). To increase the robustness, similar scRNA-Seq clusters 0 and 2 were merged, and small clusters 19 and 20 were excluded (see Methods). The integrated RNA-Seq analysis revealed three main types of composition dynamics for the cell clusters (Fig. 9).

- **Seasonal dynamics only,** without substantial reaggregation response: clusters 1, 3, 7, 11, 12, 14, and 15.
- **Depletion in reaggregation stages:** clusters 0 + 2, 6, 9, 10, 16, and 18, showing pronounced depletion, particularly in the aggregate stage.
- **Enrichment in the aggregate stage:** clusters 4, 5, 8, 13, and 17, which are more abundant in the aggregate stage than at other stages.

Deconvolution analysis revealed that, upon sponge body dissociation, cell cluster 5 decreased while clusters 0–2 increased, the opposite trend was observed in aggregates.

To further investigate transcriptional regulation of cytoskeletal plasticity during cell reaggregation in *H. dujardini*, we analyzed bulk RNA-Seq expression of actin and actin-interacting genes, including members of the Hippo/YAP and RhoA-ROCK-myosin-II pathways that coordinate cytoskele-

tal responses to mechanical stress (Supplementary Figs S19–S21, Supplementary Table S2). *HdA1/2/3* are the most highly expressed genes in *H. dujardini*, maintaining relatively stable levels during reaggregation. Under the chosen thresholds for differential expression (fold change > 1.5, FDR < 0.001; see Materials and methods), no significant changes were observed except for *HdA3* decline in Autumn dissociated cells (Supplementary Fig. S19). Generally, expression of the conserved *HdA1/2/3* demonstrated a moderate stability, underscoring an essential role in cellular maintenance and cytoskeleton organization. In contrast, divergent *HdA6* expression was an order of magnitude lower than *HdA1/2/3*, further decreasing in dissociated cells and continuing to decline in aggregates across all seasonal samples (Supplementary Fig. S19). This consistent, season-independent downregulation in aggregates suggests a specific role of *HdA6* in cellular response to mechanical stress.

The actin-associated genes, particularly cytoskeletal regulators, cross-linkers, actin monomer-binding, and nucleation proteins, demonstrated varying transcriptional responses during reaggregation. Among cross-linking proteins, Filamin-like isoforms, showed complex, season-dependent regulation. In dissociated cells from Summer samples, Filamin-like 1, 3, 8, 9, and 10 and Spectrin alpha- and beta-chains were upregulated, along with Myosin class I C. In contrast, all Filamin-like genes decreased their expression in Autumn, while in Winter, only the expression of Filamin-like 3 decreased, with Filamin-like 1 and 10 increasing. Filamin-like 5, ERM family 3, and Rho2 increased their expression under re-aggregation, while the expression of Filamin-like 8 and WAVE/WASF2 decreased across all seasons studied. Structural proteins, such as Lamin B, showed increased expression in cell aggregates across all seasons. Cytoskeletal proteins showed isoform-specific downregulation in aggregates: tubulins α1–4, α10, and β were reduced in Spring and Autumn; spectraplakin and tubulins α6–9, γ1, and γ2 decreased in all seasons except Summer; tubulins ε and α6 – across all seasons. Genes from cytoskeletal regulatory pathways exhibited notable transcriptional dynamics during reaggregation. Within the Hippo/YAP pathway, LATS, SAV1, and TEAD1 consistently increased their expression across reaggregated samples, with Yes-associated protein (YAP) specifically upregulated in Winter, Spring, and Autumn, but remaining stable in Summer. Frizzled signaling components additionally exhibited seasonal variation, with Winter samples showing increased FzdC, SFRPa, SFRPb, and SFRPc levels after dissociation. In the course of reaggregation, FzdB, FzdC, SFRPa, and SFRPb continued to rise, whereas FzdF levels decreased.

Overall, this integrated single-cell and bulk RNA-Seq analysis revealed that *H. dujardini* sponge plasticity during dissociation and aggregation relies on specific cell types, with *HdA6*-specific, pinacocyte-like clusters 5 and 8 expanding notably in cell aggregates. The moderate stability of major intronless *HdA1/2/3* isoforms expression, contrasting with the season-independent downregulation of divergent, intron-having *HdA6*, suggests distinct roles for these actins in cellular responses to mechanical stress. Seasonal and reaggregation-driven regulation of cytoskeletal components, actin-binding partners, and Rho- and Hippo/YAP-signaling proteins underscores the importance of cytoskeletal plasticity in sponge environmental adaptation and morphogenesis.

Discussion

Sponges are an early-diverging group of animals and their remarkable regenerative properties are provided by the diversity of actins and actin-associated regulatory proteins. Functional cellular heterogeneity can be determined by the expression of particular actin isoforms. Each sponge genome contains both conserved and divergent, species-specific actins (Fig. 4). The unusual actin gene organization in *H. panicea* (Fig. 1) presumably arose by duplication of an ancestral single copy gene to maximize actin synthesis [110]. A comparative analysis of the position of introns in the different actin genes of sponges with the intron positions in the actin genes from lower eukaryotes to higher eukaryotes, as well as the human actins showed an intron conservation at positions 85, 122, and 204 amino acids Supplementary Table S3). The actin genes of sponges *H. panicea*, *E.muelleri*, *A. queenslanica*, *H. dujardini* (all of them *cl. Demospongia*), *Corticium candelabrum (cl. Homoscleromorpha)*, and *S. ciliatum* (*cl. Calcarea*) have introns at the common position, around I85. This intron position is also characteristic of *Trichoplax adhaerens* (Trichoplax) and *Hydra attenuata* (Hydra) and human smooth muscle type actins (Supplementary Table S3). This feature may contribute to the common function of this actin and the vertebrate smooth muscle-type actins [19]. Another situation is found in the Ctenophora actin genes, they do not have conserved intron at I85, but have introns at G15, G168, G268 and M356. The introns at 268 aa is shared with higher animal actins, while at 356 aa is plant specific [19]. Apparently, Ctenophora represents more ancestral forms of actin genes. The only sponges *H. dujardini* (*cl. Demospongia*) and *O. minuta* (*cl. Hexactinellida*) have single intron in one actin gene (Supplementary Table S3), while the rest of their actins are intronless. Since all intronless *H. dujardini* actin genes except for *HdA5* are located on the same chromosome (Fig. 1), they could arise from gene duplication and/or retrotransposition events. It is interesting that in social amoeba *Dictyostelium discoideum* and protists *Cryptosporidium* the actin genes are intronless but have a single intron in Toxoplasma. In *Plasmodium falciparum* (Apicomplexan), there are two genes encoding actin, actin I is intronless and expresses throughout the parasite life cycle, while the actin II gene has one intron and is transcribed only at the sexual stages [111, 112]. Mammalian intronless T-ACTINs play an important role in the morphogenesis of spermatozoa during spermiogenesis, as well as in sperm function [31]. Introns probably disappeared from the actin gene to speed up the transcript processing and accumulation during differentiation of specific cells, a similar process has been described for the muscle actin gene in molgulid ascidian larvae. [110]. The functions of actin could be divided when the cell community arose for organized coexistence [56]. The divergent intron-containing *HdA6* is a more ancient paralogue, persisting in the *H. dujardini* genome despite the negative selection (Fig. 4, Supplementary Table S5). The first exon of *HdA6* is located mainly in the second subdomain of the gene. This localization of the exon is important for the proper folding and function of the actin as a molecular motor and for the interaction with myosin [102]. Intron-containing actin genes of the sponges *H. dujardini* and *O. minuta* have only the metazoan initiator (Inr) element that is required for transcription initiation of metazoan genes lacking TATA boxes. The Inr is a ubiquitous core promoter element for protein-coding genes in early eukaryotes. Analyses of the metazoan Inr indi-

cate the presence of nuclear factors which may be involved in the recognition of the Inr [113]. The only genes with CpG islands in the upstream regions were found in *HdA1* and *HdA3*, and in human *ACTB*. CpG islands are associated with diffuse transcription and regulate the expression of housekeeping genes. *Hd1* and *Hd3* are expressed in all cell clusters (Fig. 8B) and can be served as housekeeping. The differences in the structure of the 5′ regulatory sequences of the *H. dujardini* actin genes (Fig. 1) suggest that actin isoforms may be differentially expressed. Interestingly, the mRNA ratios in the nucleus and cytoplasm areas were different for actin *Hd1/2/3*, *HdA6*, and *HdA7* (Supplementary Fig. S16B), which may indirectly indicate differences in the nuclear import of these mRNAs and/or in the intensity of translation of these isoforms. Although the mRNA expression of conserved HdA1/2/3 is an order of magnitude higher than that of the divergent HdA6, both actins were found in mature and larval sponge cells. The translation repression for coordination of the different actins has been demonstrated earlier for β-actin [114].

The conserved HdA1/2/3 and divergent HdA6 were detected by LC-MS/MS in the nuclear fraction, but HdA6 was not found in the cytoplasm (Table 2). Acetylation, methylation, oxidation and ubiquitination of specific amino acids have been identified for HdA1/2/3. Ac-Gly2 amino-terminal processing and acetylation (Supplementary Fig. S12) can be involved in the dynamics of HdA1/2/3 similar to found in unicellular eukaryote actins [115–118]. The *N*-terminus of HdA6 was not identified in any of the samples examined, possibly due to its processing or detection failure. However, the *N*-termini of actin HdA1/2/3 and other proteins were found. It should be clarified in future experiments. The oxidation of methionine at M16, M44, M47, and M305 positions suggests that HdA1/2/3 actin dynamics is highly sensitive to the oxidative stress (Supplementary Fig. S12). The reversible oxidation of methionine in actin serves as a regulatory mechanism of cell adaptations [119, 120]. The oxidation of actin in endothelial cells appears to be essential for proper cell-to-cell adhesion and migration [121, 122]. The found epitope GQKDSYVGDEAQSK, the proteasome product of HdA1/2/3 actin, can be involved in the antigen presentation and important for cell-to-cell communication [123]. LC-MS/MS analysis revealed the ubiquitin (U) binding to Jasplakinolide-binding sites in HdA1/2/3 actin (Supplementary Table S6) that can stabilizes it. Jasplakinolide is a naturally occurring compound produced by symbionts of the marine sponge *Jaspis sp*, and its binding sites may be shared by other microorganisms. The same peptide sequence, SYELPDGQVIT, corresponding to the human actin at positions 241–251 aa of the unprocessed sequence has been found in prolyl isomerases (immunophilins) PIN1 of HIV-1 virions [124]. The HdA1/2/3 and HdA6 have been detected in cell ferritin complexes and granulated cells. In the previous work, we showed that the *H. dujardini* ferritin complex includes actin, tubulin, and neuroglobin [65]. Actin and tubulin are heme-binding proteins [125], and heme-binding residues were predicted in *H. dujardini* HdA1/2/3 and HdA6 and tubulin (Supplementary Table S9). The reaggregation of *H. dujardini* cells depends on the iron metabolism and is accompanied by the activation of heme biosynthesis pathway and mitochondrial activity [64, 65, 126, 127]. It is possible that these factors can regulate actin network remodeling under sponge reaggregation. The heme induces actin polymerization and promotes mammalian intestinal cell migration and proliferation regulated by NADPHox-derived ROS. The intronless *HdA1//2/3* of *H. dujardini* has features of unicellular and multicellular actin. PTMs of HdA1/2/3 actin and predicted heme-binding residues can be responsible for cell flexibility and proliferation regulated by ROS.

The cells of *H. dujardini* differ in their ROS status, F-actin distribution and sensitivity to Jasplakinolide. F-actin stabilization was observed in stellate cells and amoeboid cells with pseudopodia and active ROS states, whereas cells with long, thin outgrowths marked by punctuated F-actin did not show such stabilization. These changes may be linked to the influence of ROS on actin and suggest a potential role of this interaction in cell transformations. The diverse cell types of sponges move on different substrates using a variety of actin-dependent mechanisms controlled by actin regulators. Amoeboid-shaped cells in the sponge body or in an isolated state crawl with the help of lamellipodial protrusions formed by a branched actin network, pushing the leading edge forward, with contractility dependent on the actin and myosin regulators [128, 129]. The presence of key regulators that accelerate or inhibit the growth of actin filaments in the sponge, as well as proteins involved in the adhesion and contractility was confirmed by LC-MS/MS (Supplementary Fig. S13, Supplementary Table S2). Sponge cells can also push their leading edges of the membrane forward due to the directed flow of cytoplasm, as has been shown for some unicellular eukaryotes [130]. The motility of individual sponge cells is mediated by filopodia, linear projections filled with actin, the activity of which may be regulated in a manner similar to that of unicellular eukaryotes [131, 132]. It has been shown that different cytoplasmic actin isoforms have different distribution in mammalian cells: beta-actin was located mainly in the contractile ring, stress fibers, filopodia, and cell-cell contacts, but gamma-actin localized primarily in the cortex and lamellipodia [22, 24]. Immunofluorescence imaging revealed a magnificent F-actin staining within choanoblast clusters, which can be connected to their functional state.

Single cell profiling revealed three cell clusters in *H. dujardini* that are enriched with the expression of divergent actin gene *HdA6* (Fig. 8). Interestingly, almost all cells of the cluster 5 express *HdA6*. SAMap comparisons with the other sponges suggest these cells have expression patterns similar to those of pinacocytes. Yet, in the freshwater sponge *S. lacustris* [7] and the marine *A. queenslandica* [84] (cl. Demospongia), no clusters with differentially expressed actins were found. The coexpression of the key components of the actin-based contractile apparatus in pinacocytes was found in ScSeq of *A. queenslandica* [84]. The intriguing fact is that these cells are marked by the expression of EGFR and the EGFR-dependent pathway proteins (receptor-type tyrosine-protein phosphatase delta-like and tyrosine-protein kinase, HduFzdE) and DOMON-containing DBH-like protein. The EGFR-dependent signaling regulates differentiation of fibrocytes into a-smooth muscle actin (a-SMA)–positive myofibroblasts in the human lungs [133] and mediates Wnt-Fzd endocytosis required for intercellular communication during hematopoietic stem cell development in zebrafish [134]. The activation of the Wnt-signaling pathway associated with Frizzled proteins has been demonstrated during the development of primmorphs of sponge *H. dujardini* [135]. DOMON of DBH-like contains a conventional heme-binding pocket that functions as a cytochrome, allowing electron transfer in redox reactions. In addition, DOMON is required for noncovalent tetramerization or for

interactions with specific proteins in the secretion-associated complexes. This is extremely important for the function of adhesion proteins such as EGFR [136]. It has been shown that DBH also plays a crucial regulating role in larval metamorphosis and juvenile growth in *Sinonovacula constricta* [137]. Such efficient energy machinery ensures the function of specific cells to establish new contacts, which are important for morphogenetic processes in sponges.

Deconvolution analysis of scRNA-seq data and bulk sequencing data from samples collected in different seasons revealed opposite trends in the abundance of cluster 5 (pinacocytes) and clusters 0–2 (archaeocytes/choanocytes) under dissociation. Clusters 5 and 8, expressing *HdA6*, do not have pronounced seasonal dynamics, but the aggregates are enriched with these cell types (Fig. 9). Thus, mechanical dissociation induces cell dedifferentiation and changes the expression profile. Previous studies have demonstrated the dedifferentiation process in dissociated sponge cells [6, 57, 58, 138]. Notably, the regulation of actin-binding partners, actin cytoskeleton organization, and Rho- and Hippo/YAP-signaling pathways may differ in dissociated cells and aggregates. Interestingly, during the transition from adaptive multicellularity to the vegetative stage in *Dictyostelium discoideum*, genes involved in actin filament processes, actin cytoskeleton organization, and redox processes are misregulated via transcription factors and chromatin remodeling [16]. A similar strategy might also be used by multicellular organisms in relation to specific cell lineages. Mechanical dissociation of the sponge body has been shown to induce changes in the gene expression of actin-binding proteins (Supplementary Fig. S19). This may be due to the differences in cell polarization and the position of the nucleus, which involve actin-binding proteins and crosslinker Filamin [139], and the initiation of processes of temporary dedifferentiation of cells before their assembly into aggregates. Expression of the *HdA3* isoform decreased in the dissociated cells of autumn samples, but *HdA6* expression decreased and Lamin B increased during sponge cell reaggregation in samples of all studied periods (Supplementary Fig. S19). The increased expression of Lamin B can accelerate cell migration by inhibiting the association of the nuclear actin with the envelope to reduce nuclear movement and deformability [140]. It is possible that *HdA6* can modulate the subcellular nuclear activity of MRTF and the serum response factor (SRF). The expression of these factors is increased in cellular aggregates of sponges collected during all periods of the annual cycle studied (Supplementary Fig. S19). It is known that MRTF is a key factor determining regeneration in multicellular animals, including sponges [141, 142]. The cofactor SRF binds to the SRE in the promoter region of actin genes in vertebrates [143], and recent studies have revealed similar phenomena in invertebrates [144–146].

We observed overexpression of FzdB, FzdC, FzdE, and soluble Frizzled–related proteins SFRPa, SFRPb, SFRPc, and SFRPd that correlated with an increase of expression of Hippo/YAP-pathway proteins in cell aggregates Supplementary Fig. S20). The HippoIPPO/YAP pathway is activated under mechanotransduction [46] and is involved in angiogenesis in different animals [147], lamellipodia and filopodia formation and neuritogenesis [148]. On the other hand, the downstream effectors of Hippo/YAP signaling, YAP, are activated at a high cell density and activate TEAD expression, which activates genes promoting ferroptosis [149]. Fzd9 overexpression activates YAP and facilitates cell adhesion under stimulated osteogenesis in mammals. The 24-h spherical cell aggregates of *H. dujardini* are densely packed with cells, in which the adjustment of signaling pathways promotes their mutual retention for subsequent transformation, protecting cells from premature apoptosis. We previously found that the antiapoptotic protein BCL2 (B-Cell Leukemia/Lymphoma 2) gene expression is upregulated in *H. dujardini* cell aggregates [64, 65]. It has been shown that the BCL2 expression is activated by nuclear actin, as well as Wnt-signaling in human keratinocytes [150]. Interestingly, that mRNAs of Hd6 and tubulins are reduced in aggregates. Studies have demonstrated a specific interaction between tubulin and γ-actin in mammalian epithelial cells [151]. The mRNA expression of talin, filamin 2 and 3, small GTPases Rho, and myosin regulatory light chain MYL12 increased in sponge aggregates. The identified changes in the mRNA expression of genes for various actin-binding proteins and regulators can modulate the dynamics of cell motility and the process of establishing intercellular contacts during the formation of multicellular aggregates. Rho GTPase regulators regulate YAP [152] and F-actin depolymerization [48]. Some data defining actin network polarity and growth indicated the interplay between Arp2/3 complex (an actin polymerization nucleator) and capping protein [20]. Lamellipodia and filopodia are actin-dependent membrane protrusions at the front of the cell implicated in mesenchymal cell motility [20, 153, 154].

Thus, we discovered in sponge *H. dujardini* divergent intron-containing and conserved intronless actins that differ in gene expression profiles, PTMs, cellular and subcellular localizations, which are associated presumably with their different functions. The divergent intron-containing actin *HdA6* is differentially expressed in a specific sponge cell lineage, increasing in cell aggregates thus indicating its unique functions in the morphogenetic processes of *H. dujardini*. The molecular mechanisms governing cytoskeleton control and the presence of divergent actin in sponges can facilitate the preservation of cellular potential within aggregates, which is essential for subsequent transformations into a new integrated organism. Identifying these unique mechanisms presents an intriguing challenge for future research.

Conclusion

Although sponges lack true tissues, their bodies comprise various cell types, each characterized by unique structures and functions, which require specific actin cytoskeletal architectures. We identified both conserved and divergent actin isoforms in the spiculeless sponge *H. dujardini*, each with distinct cellular functions. The intronless HdA1/2/3 isoform serves as the primary actin, while the HdA6 is a differentially expressed divergent paralog that likely plays a unique role in morphogenesis. These findings highlight the complexity of the actin cytoskeleton in sponges and its significance in the evolution and determination of cell types.

Acknowledgements

The research was done using the equipment of the Core Centrum of the Institute of Developmental Biology RAS. The authors would like to thank the Polar Circle Tourist Center (Russia) for the help in sponge collecting.

Author contributions: Y.V.L. (Conceptualization [equal], Funding acquisition [equal], Investigation [equal], Methodol-

ogy [equal], Supervision [equal], Visualization [equal], Writing – original draft [equal], Writing – review & editing [equal]), K.I.A. (Data curation [equal], Formal Analysis [equal], Software [equal], Visualization [equal], Writing – original draft [equal], Writing – review & editing [equal]), V.M.Z. (Data curation [equal], Formal Analysis [equal], Software [equal], Visualization [equal], Writing – original draft [equal], Writing – review & editing [equal]), A.V.C. (Data curation [equal], Formal Analysis [equal], Investigation [equal], Writing – review & editing [equal]), A.V.R. (Investigation [equal], Writing – review & editing [equal]), K.V.M. (Formal Analysis [equal], Supervision [equal], Visualization [equal], Writing – original draft [equal], Writing – review & editing [equal]), S.A.G. (Investigation [equal], Visualization [equal], Writing – review & editing [equal]), A.V.B. (Investigation [equal], Visualization [equal], Writing – review & editing [equal]), A.D.F. (Investigation [equal], Visualization [equal], Writing – review & editing [equal]), P.A.E. (Investigation [equal], Writing – review & editing [equal]), M.S.S. (Formal Analysis [equal], Writing – review & editing [equal]), A.I.Z. (Formal Analysis [equal], Investigation [equal], Visualization [equal], Writing – review & editing [equal]), R.Z. (Formal Analysis [equal], Investigation [equal], Resources [equal], Visualization [equal], Writing – review & editing [equal]), N.G.G. (Investigation [equal], Writing – review & editing [equal]), V.M.I. (Investigation [equal], Writing – review & editing [equal]), A.M.K. (Formal Analysis [equal], Writing – review & editing [equal]), V.M. (Supervision [equal], Writing – review & editing [equal]), G.G. (Investigation [equal], Writing – review & editing [equal]), E.S. (Investigation [equal], Resources [equal], Writing – review & editing [equal]), O.A.G. (Investigation [equal], Resources [equal], Writing – review & editing [equal]), E.E.K. (Methodology [equal], Supervision [equal], Writing – review & editing [equal]), O.I.K. (Conceptualization [equal], Funding acquisition [equal], Investigation [equal], Methodology [equal], Project administration [equal], Supervision [equal], Visualization [equal], Writing – original draft [equal], Writing – review & editing [equal]).

Supplementary data

Supplementary data are available at NAR Genomics & Bioinformatics online.

Conflict of interest

Authors declare no conflict of interests in present work.

Funding

The work conducted under the Institute of Developmental Biology of the Russian Academy of Sciences Government Basic Research Program in 2024 (№ 0088-2024-0009).

Data availability

Sequencing data are available under NCBI BioProject accessions PRJNA594150 (bulk RNA-seq) and PRJNA1135465 (WGS, scRNA-seq).

Code that was used in the analysis (scRNA-seq data analysis, cell type deconvolution), as well as other files required for analysis reproduction, are deposited in Zenodo: doi.org/10.5281/zenodo.14981466.

References

1. Bely AE, Nyberg KG. Evolution of animal regeneration: re-emergence of a field. *Trends Ecol Evol* 2010;**25**:161–70. https://doi.org/10.1016/j.tree.2009.08.005
2. Poss KD, Tanaka EM. Hallmarks of regeneration. *Cell Stem Cell* 2024;**31**:1244–61. https://doi.org/10.1016/j.stem.2024.07.007
3. Wilson HV. On some phenomena of coalescence and regeneration in sponges. *J Exp Zool* 1907;**5**:245–58. https://doi.org/10.1002/jez.1400050204
4. Korotkova G, Movchan N. Osobennosti zashchitno-regeneratsionnykh protsessov u gubki *Halisarca dujardini* [The pecularity of the protective-regenerational processes of the sponge *Halisarca dujardini*]. *Vestn Leningr Univ* 1973;**21**:15–24.
5. Borisenko IE, Adamska M, Tokina DB *et al.* . Transdifferentiation is a driving force of regeneration in *Halisarca dujardini* (Demospongiae, Porifera). *Peer J* 2015;**3**:e1211. https://doi.org/10.7717/peerj.1211
6. Ereskovsky A, Borisenko IE, Bolshakov FV *et al.* Whole-body regeneration in sponges: diversity, fine mechanisms, and future prospects. *Genes* 2021;**12**:506. https://doi.org/10.3390/genes12040506
7. Musser JM, Schippers KJ, Nickel M *et al.* Profiling cellular diversity in sponges informs animal cell type and nervous system evolution. *Science* 2021;**374**:717–23. https://doi.org/10.1126/science.abj2949
8. Wilson HV. The behaviour of the dissociated cells in hydroids, Alcyonaria, and Asterias. *J Exp Zool* 1911;**11**:281–338.https://doi.org/10.1002/jez.1400110304
9. Liu S-Y, Selck C, Friedrich B *et al.* Reactivating head regrowth in a regeneration-deficient planarian species. *Nature* 2013;**500**:81–4. https://doi.org/10.1038/nature12414
10. Feldman M. Dissociation and reaggregation of embryonic cells of *Triturus alpestris*. *Development* 1955;**3**:251–5. https://doi.org/10.1242/dev.3.3.251
11. Xing JG, Lee LEJ, Fan L *et al.* Initiation of a zebrafish blastula cell line on rainbow trout stromal cells and subsequent development under feeder-free conditions into a cell line, ZEB2J. *Zebrafish* 2008;**5**:49–63. https://doi.org/10.1089/zeb.2007.0512
12. Asashima M, Ito Y, Chan T *et al.* In vitro organogenesis from undifferentiated cells in *Xenopus*. *Dev Dyn* 2009;**238**:1309–20. https://doi.org/10.1002/dvdy.21979
13. Moore KA, Huang S, Kong Y *et al.* Control of embryonic lung branching morphogenesis by the rho activator, cytotoxic necrotizing factor 1. *J Surg Res* 2002;**104**:95–100. https://doi.org/10.1006/jsre.2002.6418
14. Singh H, Mok P, Balakrishnan T *et al.* Up-scaling single cell-inoculated suspension culture of human embryonic stem cells. *Stem Cell Res* 2010;**4**:165–79. https://doi.org/10.1016/j.scr.2010.03.001
15. Ganeva V, Unbekandt M, Davies JA. An improved kidney dissociation and reaggregation culture system results in nephrons arranged organotypically around a single collecting duct system. *Organogenesis* 2011;**7**:83–7. https://doi.org/10.4161/org.7.2.14881
16. Wang SY, Pollina EA, Wang I-H *et al.* Role of epigenetics in unicellular to multicellular transition in Dictyostelium. *Genome Biol* 2021;**22**:134. https://doi.org/10.1186/s13059-021-02360-9
17. Szent-Györgyi A. *The Contraction of Myosin Shreads S*. New York, Budapest: Karger Basel, R. Gergely. 1942.
18. Szent-Györgyi AG. The early history of the biochemistry of muscle contraction. *J Gen Physiol* 2004;**123**:631–41. https://doi.org/10.1085/jgp.200409091
19. Bagavathi S, Malathi R. Introns and protein revolution — an analysis of the exon/intron organisation of actin genes. *FEBS Lett* 1996;**392**:63–5. https://doi.org/10.1016/0014-5793(96)00769-7
20. Blanchoin L, Boujemaa-Paterski R, Sykes C *et al.* Actin dynamics, architecture, and mechanics in cell motility. *Physiol Rev* 2014;**94**:235–63. https://doi.org/10.1152/physrev.00018.2013

21. Vedula P, Kurosaka S, MacTaggart B *et al.* Different translation dynamics of β- and γ-actin regulates cell migration. *eLife* 2021;**10**:e68712. https://doi.org/10.7554/eLife.68712
22. Dugina V, Zwaenepoel I, Gabbiani G *et al.* β- and γ-cytoplasmic actins display distinct distribution and functional diversity. *J Cell Sci* 2009;**122**:2980–8. https://doi.org/10.1242/jcs.041970
23. Gunning PW, Ghoshdastider U, Whitaker S *et al.* The evolution of compositionally and functionally distinct actin filaments. *J Cell Sci* 2015;**128**:2009–19. https://doi.org/10.1242/jcs.165563
24. Chen A, Arora PD, McCulloch CA *et al.* Cytokinesis requires localized β-actin filament production by an actin isoform specific nucleator. *Nat Commun* 2017;**8**:1530. https://doi.org/10.1038/s41467-017-01231-x
25. Boiero Sanders M, Toret CP, Guillotin A *et al.* Specialization of actin isoforms derived from the loss of key interactions with regulatory factors. *EMBO J* 2022;**41**:e107982. https://doi.org/10.15252/embj.2021107982
26. Bunnell TM, Ervasti JM. Delayed embryonic development and impaired cell growth and survival in *Actg1* null mice. *Cytoskeleton* 2010;**67**:564–72. https://doi.org/10.1002/cm.20467
27. Bunnell TM, Burbach BJ, Shimizu Y *et al.* β-Actin specifically controls cell growth, migration, and the G-actin pool. *MBoC* 2011;**22**:4047–58. https://doi.org/10.1091/mbc.e11-06-0582
28. Vedula P, Kurosaka S, Leu NA *et al.* Diverse functions of homologous actin isoforms are defined by their nucleotide, rather than their amino acid sequence. *eLife* 2017;**6**:e31661. https://doi.org/10.7554/eLife.31661
29. Mertins P, Gallwitz D. A single intronless actin gene in the fission yeast *Schizosaccharomyces pombe* : nucleotide sequence and transcripts formed in homologous and heterologous yeast. *Nucl Acids Res* 1987;**15**:7369–79. https://doi.org/10.1093/nar/15.18.7369
30. Sehring IM, Mansfeld J, Reiner C *et al.* The actin multigene family of *Paramecium tetraurelia*. *BMC Genomics* 2007;**8**:82. https://doi.org/10.1186/1471-2164-8-82
31. Tanaka H, Miyagawa Y, Tsujimura A *et al.* Genetic polymorphisms within the intronless ACTL7A and ACTL7B genes encoding spermatogenesis-specific actin-like proteins in Japanese males. *Int J Fertil Steril* 2019;**13**:245–9.
32. Liu Z, Moav B, Faras AJ *et al.* Importance of the CArG box in regulation of β-actin-encoding genes. *Gene* 1991;**108**:211–7. https://doi.org/10.1016/0378-1119(91)90436-F
33. Xu M, Gonzalez-Hurtado E, Martinez E. Core promoter-specific gene regulation: TATA box selectivity and Initiator-dependent bi-directionality of serum response factor-activated transcription. *Biochim Biophys Acta* 2016;**1859**:553–63. https://doi.org/10.1016/j.bbagrm.2016.01.005
34. Mohun TJ, Garrett N. An amphibian cytoskeletal-type actin gene is expressed exclusively in muscle tissue. *Development* 1987;**101**:393–402. https://doi.org/10.1242/dev.101.2.393
35. Stuven T. Exportin 6: a novel nuclear export receptor that is specific for profilin{middle dot}actin complexes. *EMBO J* 2003;**22**:5928–40. https://doi.org/10.1093/emboj/cdg565
36. Dopie J, Skarp K-P, Kaisa Rajakylä E *et al.* Active maintenance of nuclear actin by importin 9 supports transcription. *Proc Natl Acad Sci USA* 2012;**109**:E544–52. https://doi.org/10.1073/pnas.1118880109
37. Miyamoto K, Teperek M, Yusa K *et al.* Nuclear Wave1 is required for reprogramming transcription in oocytes and for normal development. *Science* 2013;**341**:1002–5. https://doi.org/10.1126/science.1240376
38. Redza-Dutordoir M, Averill-Bates DA. Activation of apoptosis signalling pathways by reactive oxygen species. *Biochim Biophys Acta Mol Cell Res* 2016;**1863**:2977–92. https://doi.org/10.1016/j.bbamcr.2016.09.012
39. Ishimoto T, Mori H. Control of actin polymerization via reactive oxygen species generation using light or radiation. *Front Cell Dev Biol* 2022;**10**:1014008. https://doi.org/10.3389/fcell.2022.1014008
40. Kashina A. Protein arginylation, a global biological regulator that targets actin cytoskeleton and the muscle. *Anat Rec* 2014;**297**:1630–6. https://doi.org/10.1002/ar.22969
41. Wolf K, Te Lindert M, Krause M *et al.* Physical limits of cell migration: control by ECM space and nuclear deformation and tuning by proteolysis and traction force. *J Cell Biol* 2013;**201**:1069–84. https://doi.org/10.1083/jcb.201210152
42. Sanz-Moreno V, Marshall CJ. The plasticity of cytoskeletal dynamics underlying neoplastic cell migration. *Curr Opin Cell Biol* 2010;**22**:690–6. https://doi.org/10.1016/j.ceb.2010.08.020
43. Petrie RJ, Yamada KM. At the leading edge of three-dimensional cell migration. *J Cell Sci* 2012;**125**:5917–26. https://doi.org/10.1242/jcs.093732
44. Peyton SR, Ghajar CM, Khatiwala CB *et al.* The emergence of ECM mechanics and cytoskeletal tension as important regulators of cell function. *Cell Biochem Biophys* 2007;**47**:300–20. https://doi.org/10.1007/s12013-007-0004-y
45. Roca-Cusachs P, Iskratsch T, Sheetz MP. Finding the weakest link – exploring integrin-mediated mechanical molecular pathways. *J Cell Sci* 2012;**125**:3025–38. https://doi.org/10.1242/jcs.095794
46. Janmey PA, Fletcher DA, Reinhart-King CA. Stiffness sensing by cells. *Physiol Rev* 2020;**100**:695–724. https://doi.org/10.1152/physrev.00013.2019
47. Phillips JE, Zheng Y, Pan D. Assembling a hippo: the evolutionary emergence of an animal developmental signaling pathway. *Trends Biochem Sci* 2024;**49**:681–92. https://doi.org/10.1016/j.tibs.2024.04.005
48. Piccolo S, Dupont S, Cordenonsi M. The Biology of YAP/TAZ: hippo signaling and beyond. *Physiol Rev* 2014;**94**:1287–312. https://doi.org/10.1152/physrev.00005.2014
49. Dupont S, Morsut L, Aragona M *et al.* Role of YAP/TAZ in mechanotransduction. *Nature* 2011;**474**:179–83. https://doi.org/10.1038/nature10137
50. Rivero F, Xiong H. Rho signaling in *Dictyostelium discoideum*. In: *International Review of Cell and Molecular Biology*. Amsterdam, the Netherlands: Elsevier, 2016, **322**, 61–181.
51. Ketelaar T, Meijer HJG, Spiekerman M *et al.* Effects of latrunculin B on the actin cytoskeleton and hyphal growth in Phytophthora infestans. *Fung Genet Biol* 2012;**49**:1014–22. https://doi.org/10.1016/j.fgb.2012.09.008
52. Parisis N, Krasinska L, Harker B *et al.* Initiation of DNA replication requires actin dynamics and formin activity. *EMBO J* 2017;**36**:3212–31. https://doi.org/10.15252/embj.201796585
53. Lenz KD, Klosterman KE, Mukundan H *et al.* Macrolides: from toxins to therapeutics. *Toxins* 2021;**13**:347. https://doi.org/10.3390/toxins13050347
54. Ereskovsky AV. *The Comparative Embryology of Sponges*, Dordrecht: Springer, the Netherlands. 2010. https://doi.org/10.1007/978-90-481-8575-7
55. Simpson TL. *The Cell Biology of Sponges*. New York, NY: Springer New York, 1984. https://doi.org/10.1007/978-1-4612-5214-6
56. Sogabe S, Hatleberg WL, Kocot KM *et al.* Pluripotency and the origin of animal multicellularity. *Nature* 2019;**570**:519–22. https://doi.org/10.1038/s41586-019-1290-4
57. Soubigou A, Ross EG, Touhami Y *et al.* Regeneration in sponge *Sycon ciliatum* partly mimics postlarval development. *Development* 2020;**147**:dev193714. https://doi.org/10.1242/dev.193714
58. Golyshev SA, Lyupina YV, Kravchuk OI *et al.* Transient interphase microtubules appear in differentiating sponge cells. *Cells* 2024;**13**:736. https://doi.org/10.3390/cells13090736
59. Colgren J, Nichols SA. MRTF specifies a muscle-like contractile module in Porifera. *Nat Commun* 2022;**13**:4134. https://doi.org/10.1038/s41467-022-31756-9
60. Ereskovsky AV, Gonobobleva E, Vishnyakov A. Morphological evidence for vertical transmission of symbiotic bacteria in the

viviparous sponge *Halisarca dujardini* Johnston (Porifera, Demospongiae, Halisarcida). *Mar Biol* 2005;**146**:869–75. https://doi.org/10.1007/s00227-004-1489-1
61. Aktories K, Lang AE, Schwan C *et al.* Actin as target for modification by bacterial protein toxins. *FEBS J* 2011;**278**:4526–43. https://doi.org/10.1111/j.1742-4658.2011.08113.x
62. Navarro-Garcia F, Serapio-Palacios A, Ugalde-Silva P *et al.* Actin cytoskeleton manipulation by effector proteins secreted by diarrheagenic *Escherichia coli* pathotypes. *Biomed Res Int* 2013;**2013**:374395. https://doi.org/10.1155/2013/374395
63. Ehrlich H, Luczak M, Ziganshin R *et al.* Arrested in glass: actin within sophisticated architectures of biosilica in sponges. *Adv Sci* 2022;**9**:2105059. https://doi.org/10.1002/advs.202105059
64. Finoshin AD, Adameyko KI, Mikhailov KV *et al.* Iron metabolic pathways in the processes of sponge plasticity. *PLoS One* 2020;**15**:e0228722. https://doi.org/10.1371/journal.pone.0228722
65. Adameyko KI, Burakov AV, Finoshin AD *et al.* Conservative and *Atypical Ferritins* of Sponges. *Int J Mol Sci* 2021;**22**:8635. https://doi.org/10.3390/ijms22168635
66. Ereskovsky AV, Gonobobleva EL. New data on embryonic development of *Halisarca dujardini* Johnston, 1842 (Demospongiae, Halisarcida). *Zoosystema* 2000;**22**:355–68.
67. Smale ST, Kadonaga JT. The RNA Polymerase II Core Promoter. *Annu. Rev. Biochem.* 2003;**72**:449–79. https://doi.org/10.1146/annurev.biochem.72.121801.161520
68. Benoist C, O'Hare K, Breathnach R *et al.* The ovalbumin gene - sequence of putative control regions. *Nucleus Acids Res* 1980;**8**:127–42. https://doi.org/10.1093/nar/8.1.127
69. Efstratiadis A. The structure and evolution of the human β-globin gene family. *Cell* 1980;**21**:653–68. https://doi.org/10.1016/0092-8674(80)90429-8
70. Nakajima-Iijima S, Hamada H, Reddy P *et al.* Molecular structure of the human cytoplasmic beta-actin gene: interspecies homology of sequences in the introns. *Proc Natl Acad Sci USA* 1985;**82**:6133–7. https://doi.org/10.1073/pnas.82.18.6133
71. Kumar MS, Hendrix JA, Johnson AD *et al.* Smooth muscle α-actin gene requires two E-boxes for proper expression *in vivo* and is a target of class I basic helix-loop-helix proteins. *Circ Res* 2003;**92**:840–7. https://doi.org/10.1161/01.RES.0000069031.55281.7C
72. Rice P, Longden I, Bleasby A. EMBOSS: the European Molecular Biology Open Software Suite. *Trends Genet* 2000;**16**:276–7. https://doi.org/10.1016/S0168-9525(00)02024-2
73. Emms DM, Kelly S. OrthoFinder: phylogenetic orthology inference for comparative genomics. *Genome Biol* 2019;**20**:238. https://doi.org/10.1186/s13059-019-1832-y
74. Katoh K, Standley DM. MAFFT Multiple Sequence Alignment Software Version 7: improvements in performance and usability. *Mol Biol Evol* 2013;**30**:772–80. https://doi.org/10.1093/molbev/mst010
75. Capella-Gutiérrez S, Silla-Martínez JM, Gabaldón T. trimAl: a tool for automated alignment trimming in large-scale phylogenetic analyses. *Bioinformatics* 2009;**25**:1972–3. https://doi.org/10.1093/bioinformatics/btp348
76. Lartillot N, Rodrigue N, Stubbs D *et al.* PhyloBayes MPI: phylogenetic reconstruction with infinite mixtures of profiles in a parallel environment. *Syst Biol* 2013;**62**:611–5. https://doi.org/10.1093/sysbio/syt022
77. Kumar S, Stecher G, Tamura K. MEGA7: molecular evolutionary genetics analysis version 7.0 for bigger datasets. *Mol Biol Evol* 2016;**33**:1870–4. https://doi.org/10.1093/molbev/msw054
78. Letunic I, Bork P. Interactive Tree of Life (iTOL) v6: recent updates to the phylogenetic tree display and annotation tool. *Nucleic Acids Res* 2024;**52**:W78–82. https://doi.org/10.1093/nar/gkae268
79. Abascal F, Zardoya R, Telford MJ. TranslatorX: multiple alignment of nucleotide sequences guided by amino acid translations. *Nucleic Acids Res* 2010;**38**:W7–W13. https://doi.org/10.1093/nar/gkq291
80. Zheng GXY, Terry JM, Belgrader P *et al.* Massively parallel digital transcriptional profiling of single cells. *Nat Commun* 2017;**8**:14049. https://doi.org/10.1038/ncomms14049
81. Kayal E, Lavrov DV. The mitochondrial genome of Hydra oligactis (Cnidaria, Hydrozoa) sheds new light on animal mtDNA evolution and cnidarian phylogeny. *Gene* 2008;**410**:177–86. https://doi.org/10.1016/j.gene.2007.12.002
82. Haese-Hill W, Crouch K, Otto TD. peaks2utr: a robust Python tool for the annotation of 3′ UTRs. *Bioinformatics* 2023;**39**:btad112. https://doi.org/10.1093/bioinformatics/btad112
83. Tarashansky AJ, Musser JM, Khariton M *et al.* Mapping single-cell atlases throughout Metazoa unravels cell type evolution. *eLife* 2021;**10**:e66747. https://doi.org/10.7554/eLife.66747
84. Sebé-Pedrós A, Chomsky E, Pang K *et al.* Early metazoan cell type diversity and the evolution of multicellular gene regulation. *Nat Ecol Evol* 2018;**2**:1176–88. https://doi.org/10.1038/s41559-018-0575-6
85. Dobin A, Davis CA, Schlesinger F *et al.* STAR: ultrafast universal RNA-seq aligner. *Bioinformatics* 2013;**29**:15–21. https://doi.org/10.1093/bioinformatics/bts635
86. Wang X, Park J, Susztak K *et al.* Bulk tissue cell type deconvolution with multi-subject single-cell expression reference. *Nat Commun* 2019;**10**:380. https://doi.org/10.1038/s41467-018-08023-x
87. Bates DM. lme4: mixed-effects modeling with R. https://www.jstatsoft.org/article/view/v067i01 (13 May 2025,date last accessed).
88. Liao Y, Smyth GK, Shi W. featureCounts: an efficient general purpose program for assigning sequence reads to genomic features. *Bioinformatics* 2014;**30**:923–30. https://doi.org/10.1093/bioinformatics/btt656
89. McCarthy DJ, Chen Y, Smyth GK. Differential expression analysis of multifactor RNA-Seq experiments with respect to biological variation. *Nucleic Acids Res* 2012;**40**:4288–97. https://doi.org/10.1093/nar/gks042
90. Gu Z, Eils R, Schlesner M. Complex heatmaps reveal patterns and correlations in multidimensional genomic data. *Bioinformatics* 2016;**32**:2847–9. https://doi.org/10.1093/bioinformatics/btw313
91. Schmidt WM, Mueller MW. CapSelect: a highly sensitive method for 5' CAP-dependent enrichment of full-length cDNA in PCR-mediated analysis of mRNAs. *Nucleic Acids Res* 1999;**27**:i–iv. https://doi.org/10.1093/nar/27.21.e31-i
92. Matz M. Amplification of cDNA ends based on template-switching effect and step- out PCR. *Nucleic Acids Res* 1999;**27**:1558–60. https://doi.org/10.1093/nar/27.6.1558
93. Huff J. The Fast mode for ZEISS LSM 880 with Airyscan: high-speed confocal imaging with super-resolution and improved signal-to-noise ratio. *Nat Methods* 2016;**13**:i–ii. https://doi.org/10.1038/nmeth.f.398
94. Camacho C, Coulouris G, Avagyan V *et al.* BLAST+: architecture and applications. *BMC Bioinf* 2009;**10**:421. https://doi.org/10.1186/1471-2105-10-421
95. Slater GSC, Birney E. Automated generation of heuristics for biological sequence comparison. *BMC Bioinf* 2005;**6**:31. https://doi.org/10.1186/1471-2105-6-31
96. Paysan-Lafosse T, Blum M, Chuguransky S *et al.* InterPro in 2022. *Nucleic Acids Res* 2023;**51**:D418–27. https://doi.org/10.1093/nar/gkac993
97. Wang J, Chitsaz F, Derbyshire MK *et al.* The conserved domain database in 2023. *Nucleic Acids Res* 2023;**51**:D384–8. https://doi.org/10.1093/nar/gkac1096
98. Sievers F, Higgins DG. Clustal Omega for making accurate alignments of many protein sequences. *Protein Sci* 2018;**27**:135–45. https://doi.org/10.1002/pro.3290

99. Robert X, Gouet P. Deciphering key features in protein structures with the new ENDscript server. *Nucleic Acids Res* 2014;**42**:W320–4. https://doi.org/10.1093/nar/gku316
100. Waterhouse AM, Procter JB, Martin DMA *et al.* Jalview Version 2—a multiple sequence alignment editor and analysis workbench. *Bioinformatics* 2009;**25**:1189–91. https://doi.org/10.1093/bioinformatics/btp033
101. Khaitlina SY, Strzelecka-Gołaszewska H. Role of the DNase-I-binding loop in dynamic properties of actin filament. *Biophys J* 2002;**82**:321–34. https://doi.org/10.1016/S0006-3495(02)75397-6
102. Dominguez R, Holmes KC. Actin structure and function. *Annu Rev Biophys* 2011;**40**:169–86. https://doi.org/10.1146/annurev-biophys-042910-155359
103. Tikhomirova TS, Ievlev RS, Suvorina MY *et al.*. Search for functionally significant motifs and amino acid residues of actin. *Mol Biol* 2018;**52**:118–35. https://doi.org/10.1134/S0026893318010193
104. Paul George AA, Lacerda M, Sylwasschy BF *et al.* HeMoQuest: a webserver for qualitative prediction of transient heme binding to protein motifs. *BMC Bioinf* 2020;**21**:124. https://doi.org/10.1186/s12859-020-3420-2
105. Waterhouse A, Bertoni M, Bienert S *et al.* SWISS-MODEL: homology modelling of protein structures and complexes. *Nucleic Acids Res* 2018;**46**:W296–303. https://doi.org/10.1093/nar/gky427
106. Abramson J, Adler J, Dunger J *et al.* Accurate structure prediction of biomolecular interactions with AlphaFold 3. *Nature* 2024;**630**:493–500. https://doi.org/10.1038/s41586-024-07487-w
107. Schrödinger LLC. *The PyMOL Molecular Graphics System*. Version 1.8. Schrödinger, LLC: New York, NY, USA. https://pymol.org/ (13 May 2025, date last accessed).
108. Ma B, Zhang K, Hendrie C *et al.* PEAKS: powerful software for peptide *de novo* sequencing by tandem mass spectrometry. *Rapid Comm Mass Spectrom* 2003;**17**:2337–42. https://doi.org/10.1002/rcm.1196
109. Wu Y, Wei B, Liu H *et al.* MiRPara: a SVM-based software tool for prediction of most probable microRNA coding regions in genome scale sequences. *BMC Bioinf* 2011;**12**:107. https://doi.org/10.1186/1471-2105-12-107
110. Kusakabe T. Ascidian actin genes: developmental regulation of gene expression and molecular evolution. *Zoolog Sci* 1997;**14**:707–18. https://doi.org/10.2108/zsj.14.707
111. Wesseling JG, Snijders PJF, Van Someren P *et al.* Stage-specific expression and genomic organization of the actin genes of the malaria parasite *Plasmodium falciparum*. *Mol Biochem Parasitol* 1989;**35**:167–76. https://doi.org/10.1016/0166-6851(89)90119-9
112. Cevallos AM, López-Villaseñor I, Espinosa N *et al.* Trypanosoma cruzi: allelic comparisons of the actin genes and analysis of their transcripts. *Exp Parasitol* 2003;**103**:27–34. https://doi.org/10.1016/S0014-4894(03)00066-3
113. Liston DR, Johnson PJ. Analysis of a ubiquitous promoter element in a primitive eukaryote: early evolution of the initiator element. *Mol Cell Biol* 1999;**19**:2380–8. https://doi.org/10.1128/MCB.19.3.2380
114. Zhang F, Saha S, Shabalina SA *et al.* Differential arginylation of actin isoforms is regulated by coding sequence–dependent degradation. *Science* 2010;**329**:1534–7. https://doi.org/10.1126/science.1191701
115. Redman K, Rubenstein PA. NH2-terminal processing of *Dictyostelium discoideum* actin *in vitro*. *J Biol Chem* 1981;**256**:13226–9. https://doi.org/10.1016/S0021-9258(18)43032-3
116. Rubenstein PA. The functional importance of multiple actin isoforms. *Bioessays* 1990;**12**:309–15. https://doi.org/10.1002/bies.950120702
117. Vahokoski J, Bhargav SP, Desfosses A *et al.* Structural differences explain diverse functions of plasmodium actins. *PLoS Pathog* 2014;**10**:e1004091. https://doi.org/10.1371/journal.ppat.1004091
118. Manich M, Hernandez-Cuevas N, Ospina-Villa JD *et al.* Morphodynamics of the actin-rich cytoskeleton in *Entamoeba histolytica*. *Front Cell Infect Microbiol* 2018;**8**:179. https://doi.org/10.3389/fcimb.2018.00179
119. Hung R-J, Pak CW, Terman JR. Direct redox regulation of F-actin assembly and disassembly by mical. *Science* 2011;**334**:1710–3. https://doi.org/10.1126/science.1211956
120. Lim JM, Kim G, Levine RL. Methionine in Proteins: it's not just for protein initiation anymore. *Neurochem Res* 2019;**44**:247–57. https://doi.org/10.1007/s11064-017-2460-0
121. Moldovan L, Moldovan NI, Sohn RH *et al.* Redox changes of cultured endothelial cells and actin dynamics. *Circ Res* 2000;**86**:549–57. https://doi.org/10.1161/01.RES.86.5.549
122. Fiaschi T, Cozzi G, Raugei G *et al.* Redox regulation of β-Actin during integrin-mediated cell adhesion. *J Biol Chem* 2006;**281**:22983–91. https://doi.org/10.1074/jbc.M603040200
123. Stocki P, Morris NJ, Preisinger C *et al.* Identification of potential HLA class I and class II epitope precursors associated with heat shock protein 70 (HSPA). *Cell Stress Chaperones* 2010;**15**:729–41. https://doi.org/10.1007/s12192-010-0184-z
124. Ott DE, Coren LV, Johnson DG *et al.* Actin-binding cellular proteins inside human immunodeficiency virus type 1. *Virology* 2000;**266**:42–51. https://doi.org/10.1006/viro.1999.0075
125. Li X, Wang X, Zhao K *et al.* A novel approach for identifying the heme-binding proteins from mouse tissues. *Genom Proteom Bioinform* 2003;**1**:78–86. https://doi.org/10.1016/S1672-0229(03)01011-8
126. Adameyko KI, Kravchuk OI, Finoshin AD *et al.* Structure of neuroglobin from cold-water sponge *Halisarca dujardinii*. *Mol Biol* 2020;**54**:416–20. https://doi.org/10.1134/S0026893320030036
127. Kravchuk OI, Finoshin AD, Mikhailov KV *et al.* Characteristics of δ-aminolevulinic acid dehydratase of the cold-water sponge *Halisarca dujardinii*. *Mol Biol* 2023;**57**:1085–96. https://doi.org/10.1134/S0026893323060109
128. Olguin-Olguin A, Aalto A, Maugis B *et al.* Chemokine-biased robust self-organizing polarization of migrating cells in vivo. *Proc Natl Acad Sci USA* 2021;**118**:e2018480118. https://doi.org/10.1073/pnas.2018480118
129. Stroka KM, Jiang H, Chen S-H *et al.* Water permeation drives tumor cell migration in confined microenvironments. *Cell* 2014;**157**:611–23. https://doi.org/10.1016/j.cell.2014.02.052
130. Taniguchi A, Nishigami Y, Kajiura-Kobayashi H *et al.* Light-sheet microscopy reveals dorsoventral asymmetric membrane dynamics of *Amoeba proteus* during pressure-driven locomotion. *Biol Open* 2023;**12**:bio059671. https://doi.org/10.1242/bio.059671
131. Dayel MJ, Alegado RA, Fairclough SR *et al.* Cell differentiation and morphogenesis in the colony-forming choanoflagellate Salpingoeca rosetta. *Dev Biol* 2011;**357**:73–82. https://doi.org/10.1016/j.ydbio.2011.06.003
132. Parra-Acero H, Harcet M, Sánchez-Pons N *et al.* Integrin-mediated adhesion in the unicellular Holozoan Capsaspora owczarzaki. *Curr Biol* 2020;**30**:4270–5. https://doi.org/10.1016/j.cub.2020.08.015
133. Wang C-H, Huang C-D, Lin H-C *et al.* Increased activation of fibrocytes in patients with chronic obstructive asthma through an epidermal growth factor receptor–dependent pathway. *J Allergy Clin Immunol* 2012;**129**:1367–76. https://doi.org/10.1016/j.jaci.2012.01.038
134. Nguyen N, Carpenter KA, Ensing J *et al.* EGFR-dependent endocytosis of Wnt9a and Fzd9b promotes β-catenin signaling during hematopoietic stem cell development in zebrafish. *Sci Signal* 2024;**17**:eadf4299. https://doi.org/10.1126/scisignal.adf4299

135. Borisenko I, Bolshakov FV, Ereskovsky A *et al.* Expression of Wnt and TGF-beta pathway components during whole-body regeneration from cell aggregates in Demosponge *Halisarca dujardinii*. *Genes* 2021;**12**:944. https://doi.org/10.3390/genes12060944
136. Aravind L. DOMON: an ancient extracellular domain in dopamine. *Trends Biochem Sci* 2001;**26**:524–6. https://doi.org/10.1016/S0968-0004(01)01924-7
137. Li Z, Niu D, Peng M *et al.* Dopamine beta-hydroxylase and its role in regulating the growth and larval metamorphosis in *Sinonovacula constricta*. *Gene* 2020;**737**:144418. https://doi.org/10.1016/j.gene.2020.144418
138. Riesgo A, Santodomingo N, Koutsouveli V *et al.* Molecular machineries of ciliogenesis, cell survival, and vasculogenesis are differentially expressed during regeneration in explants of the demosponge *Halichondria panicea*. *BMC Genom* 2022;**23**:858. https://doi.org/10.1186/s12864-022-09035-0
139. Davidson PM, Cadot B. Actin on and around the nucleus. *Trends Cell Biol* 2021;**31**:211–23. https://doi.org/10.1016/j.tcb.2020.11.009
140. Fracchia A, Asraf T, Salmon-Divon M *et al.* Increased lamin B1 levels promote cell migration by altering perinuclear actin organization. *Cells* 2020;**9**:2161. https://doi.org/10.3390/cells9102161
141. Song R, Zhao S, Xu Y *et al.* MRTF-A regulates myoblast commitment to differentiation by targeting PAX7 during muscle regeneration. *J Cell Mol Med* 2021;**25**:8645–61. https://doi.org/10.1111/jcmm.16820
142. Han W, Chu Q, Li J *et al.* Modulating myofibroblastic differentiation of fibroblasts through Actin-MRTF signaling axis by micropatterned surfaces for suppressed implant-induced fibrosis. *Research* 2023;**6**:0049. https://doi.org/10.34133/research.0049
143. Miano JM, Long X, Fujiwara K. Serum response factor: master regulator of the actin cytoskeleton and contractile apparatus. *Am J Physiol Cell Physiol* 2007;**292**:C70–81.
144. Fukushige T, Brodigan TM, Schriefer LA *et al.* Defining the transcriptional redundancy of early bodywall muscle development in *C. elegans*: evidence for a unified theory of animal muscle development. *Genes Dev.* 2006;**20**:3395–406. https://doi.org/10.1101/gad.1481706
145. Adema CM, Hillier LW, Jones CS *et al.* Whole genome analysis of a schistosomiasis-transmitting freshwater snail. *Nat Commun* 2017;**8**:15451. https://doi.org/10.1038/ncomms15451
146. DeAguero AA, Castillo L, Oas ST *et al.* Regulation of fiber-specific actin expression by the *Drosophila* SRF ortholog blistered. *Development* 2019;**146**:dev164129. https://doi.org/10.1242/dev.164129
147. Boopathy GTK, Hong W. Role of hippo pathway-YAP/TAZ signaling in angiogenesis. *Front Cell Dev Biol* 2019;**7**:49. https://doi.org/10.3389/fcell.2019.00049
148. Antón IM, Wandosell F. WIP, YAP/TAZ and actin connections orchestrate development and transformation in the central nervous system. *Front Cell Dev Biol* 2021;**9**:673986. https://doi.org/10.3389/fcell.2021.673986
149. Meng Y, Sun H, Li Y *et al.* Targeting ferroptosis by ubiquitin system enzymes: a potential therapeutic strategy in cancer. *Int J Biol Sci* 2022;**18**:5475–88. https://doi.org/10.7150/ijbs.73790
150. Sharili AS, Kenny FN, Vartiainen MK *et al.* Nuclear actin modulates cell motility via transcriptional regulation of adhesive and cytoskeletal genes. *Sci Rep* 2016;**6**:33893. https://doi.org/10.1038/srep33893
151. Dugina V, Alieva I, Khromova N *et al.* Interaction of microtubules with the actin cytoskeleton via cross-talk of EB1-containing +TIPs and γ-actin in epithelial cells. *Oncotarget* 2016;**7**:72699–715. https://doi.org/10.18632/oncotarget.12236
152. Yu F-X, Zhao B, Panupinthu N *et al.* Regulation of the Hippo-YAP pathway by G-protein-coupled receptor signaling. *Cell* 2012;**150**:780–91. https://doi.org/10.1016/j.cell.2012.06.037
153. Svitkina TM, Borisy GG. Arp2/3 complex and actin depolymerizing factor/cofilin in dendritic organization and treadmilling of actin filament array in lamellipodia. *J Cell Biol* 1999;**145**:1009–26. https://doi.org/10.1083/jcb.145.5.1009
154. Yang C, Svitkina T. Filopodia initiation: focus on the Arp2/3 complex and formins. *Cell Adh Migr* 2011;**5**:402–8. https://doi.org/10.4161/cam.5.5.16971

Received: November 13, 2024. **Revised:** March 6, 2025. **Editorial Decision:** May 12, 2025. **Accepted:** May 16, 2025